Journal of Computational Physics 229 (2010) 3706–3725

Contents lists available at ScienceDirect

Journal of Computational Physics

journal homepage: www.elsevier.com/locate/jcp

Bandgap optimization of two-dimensional photonic crystals using semidefinite programming and subspace methods ☆

H. Men [a], N.C. Nguyen [b,*], R.M. Freund [c], P.A. Parrilo [d], J. Peraire [b]

[a] National University of Singapore, Center for Singapore-MIT Alliance, Singapore 117576, Singapore
[b] MIT Department of Aeronautics and Astronautics, 77 Massachusetts Ave., Cambridge, MA 02139, USA
[c] MIT Sloan School of Management, 50 Memorial Drive, Cambridge, MA 02142, USA
[d] MIT Department of Electrical Engineering and Computer Science, 77 Massachusetts Ave., Cambridge, MA 02139, USA

ARTICLE INFO

Article history:
Received 11 July 2009
Received in revised form 16 January 2010
Accepted 18 January 2010
Available online 28 January 2010

Keywords:
Photonic crystals
Semidefinite programming
Subspace methods
Bandgap optimization

ABSTRACT

In this paper, we consider the optimal design of photonic crystal structures for two-dimensional square lattices. The mathematical formulation of the bandgap optimization problem leads to an infinite-dimensional Hermitian eigenvalue optimization problem parametrized by the dielectric material and the wave vector. To make the problem tractable, the original eigenvalue problem is discretized using the finite element method into a series of finite-dimensional eigenvalue problems for multiple values of the wave vector parameter. The resulting optimization problem is large-scale and non-convex, with low regularity and non-differentiable objective. By restricting to appropriate eigenspaces, we reduce the large-scale non-convex optimization problem via reparametrization to a sequence of small-scale convex semidefinite programs (SDPs) for which modern SDP solvers can be efficiently applied. Numerical results are presented for both transverse magnetic (TM) and transverse electric (TE) polarizations at several frequency bands. The optimized structures exhibit patterns which go far beyond typical physical intuition on periodic media design.

1. Introduction

The propagation of waves in periodic media has attracted considerable interest in recent years. This interest stems from the possibility of creating periodic structures that exhibit bandgaps in their spectrum, i.e., frequency regions in which the wave propagation is prohibited. Bandgaps occur in many wave propagation phenomena including electromagnetic, acoustic and elastic waves. Periodic structures exhibiting electromagnetic wave bandgaps, or photonic crystals, have proven very important as device components for integrated optics including frequency filters [11], waveguides [10], switches [21], and optical buffers [28].

The optimal conditions for the appearance of gaps were first studied for one-dimensional crystals by Lord Rayleigh in 1887 [18]. In a one-dimensional periodic structure, one can widen the bandgap by increasing the contrast in the refractive index and difference in width between the materials. Furthermore, it is possible to create bandgaps for any particular frequency by changing the periodicity length of the crystal. Unfortunately, however, in two or three dimensions one can only suggest rules of thumb for the existence of a bandgap in a periodic structure, since no rigorous criteria have yet been determined. This made the design of two- or three-dimensional crystals a trial and error process, being far from optimal. Indeed,

☆ This research has been supported through AFOSR Grant FA9550-08-1-0350 and the Singapore-MIT Alliance.
* Corresponding author. Tel.: +1 617 253 8080.
E-mail addresses: men@nus.edu.sg (H. Men), cuongng@mit.edu (N.C. Nguyen), rfreund@mit.edu (R.M. Freund), parrilo@mit.edu (P.A. Parrilo), peraire@mit.edu (J. Peraire).

0021-9991/$ - see front matter © 2010 Elsevier Inc. All rights reserved.
doi:10.1016/j.jcp.2010.01.023

the possibility of two- and three-dimensionally periodic crystals with corresponding two- and three-dimensional bandgaps was not suggested until 100 years after Rayleigh's discovery of photonic bandgap in one dimension, by Yablonovitch [26] and John [14] in 1987.

From a mathematical viewpoint, the calculation of the bandgap reduces to the solution of an infinite-dimensional Hermitian eigenvalue problem which is parametrized by the dielectric function and the wave vector. In the design setting, however, one wishes to know the answer to the question: which periodic structures, composed of arbitrary arrangements of two or more different materials, produce the largest bandgaps around a certain frequency? This question can be rigorously addressed by formulating an optimization problem for the parameters that represent the material properties and geometry of the periodic structure. The resulting problem is infinite-dimensional with an infinite number of constraints. After appropriate discretization in space and consideration of a finite set of wave vectors, one obtains a large-scale finite-dimensional eigenvalue problem which is non-convex and is known to be non-differentiable when eigenvalue multiplicities exist. The current state-of-the-art work done on this problem falls into two broad categories. The first kind tries to find the "optimal" band structure by parameter studies – based on prescribed inclusion shapes (e.g., circular or hexagonal inclusions) [9], fixed topology [27], or geometric considerations from the interpretation of an extensive numerical optimization study [19]. The second kind attempts to use formal topology optimization techniques [4,7,20], and level set methods [15]. Both approaches typically use gradient-based optimization methods. While these methods are attractive and have been quite successful in practice, the optimization processes employed explicitly compute the sensitivities of eigenvalues with respect to the dielectric function, which are local subgradients for such non-differentiable problem. As a result, gradient-based solution methods often suffer from the lack of regularity of the underlying problem when eigenvalue multiplicities are present, as they typically are at or near the solution.

In this paper we propose a new approach based on semidefinite programming (SDP) and subspace methods for the optimal design of photonic band structure. In the last two decades, SDP has emerged as the most important class of models in convex optimization; see [1,2,16,23,25]. SDP encompasses a huge array of convex problems as special cases, and is computationally tractable (usually comparable to least-square problems of comparable dimensions). There are three distinct properties that make SDP very suitable for the bandgap optimization problem. First, the underlying differential operator is Hermitian and positive semidefinite. Second, the objective and associated constraints involve bounds on eigenvalues of matrices. And third, as explained below, we can approximate the original non-convex optimization problem by a semidefinite program for which SDP can be well applied, thanks to its efficiency and robustness of handling this type of spectral objective and constraints.

In our approach, we first reformulate the original problem of maximizing the bandgap between two consecutive eigenvalues as an optimization problem in which we optimize the gap in eigenvalues between two orthogonal subspaces. The first eigenspace consists of eigenfunctions corresponding to eigenvalues below the bandgap, whereas the second eigenspace consists of eigenfunctions whose eigenvalues are above the bandgap. In this way, the eigenvalues are no longer present in our formulation; however, like the original problem, the exactly reformulated optimization problem is large-scale. To reduce the problem size, we truncate the high-dimensional subspaces to only a few eigenfunctions below and above the bandgap [5,17], thereby obtaining a new small-scale yet non-convex optimization problem. Finally, we keep the subspaces fixed at a given decision parameter vector and use a reparametrization of the decision variables to obtain a convex semidefinite optimization problem for which SDP solution methods can be effectively applied. We apply this approach to optimize bandgaps in two-dimensional photonic crystals for either the transverse magnetic (TM) or the transverse electric (TE) polarizations.

A detailed assessment of the computational efficiency of the proposed approach compared to alternative methods is outside the scope of this paper. We note that the performance of methods that require sensitivity information of the eigenvalues with respect to the dielectric function will deteriorate when eigenvalue multiplicities occur. The approach developed herein is designed to deal with such situations and therefore, we expect it will perform with increased robustness in complex realistic applications.

The rest of the paper is organized as follows. In Section 2 we introduce the governing differential equations and the mathematical formulation of the bandgap optimization problem. We then discuss the discretization process and present the subspace restriction approach. In Section 3 we introduce the semidefinite programming formulation of the band structure optimization, and lay out the optimization steps involved in solving the problem. Numerical results are presented in Section 4 for both the TE and TM polarizations in square lattices. Finally, in Section 5 we conclude with several remarks on anticipated future research directions.

2. The bandgap optimization problem

2.1. Governing equations

Our primary concern is the propagation of electromagnetic linear waves in periodic media, and the design of such periodic structures, or photonic crystals, to create optimal bandgaps in their spectrum. The propagation of electromagnetic waves in photonic crystals is governed by Maxwell's equations. The solutions to these equations are in general very complex functions of space and time. Due to linearity however, it is possible to separate the time dependence from the spatial dependence by expanding the solution in terms of harmonic modes – any time-varying solution can always be reconstructed by a

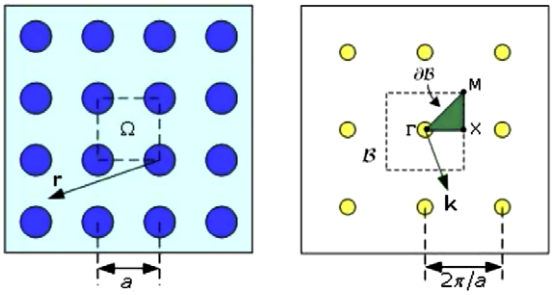

Fig. 1. Left: A photonic crystal on a square lattice. The dashed box represents the primitive unit cell (Ω), where $\boldsymbol{a}$ is the periodicity length of the lattice. Right: The reciprocal lattice, and the dashed box represents the first Brillouin zone ($\mathcal{B}$). The irreducible zone is the green triangular wedge, and its boundary is denoted by $\partial\mathcal{B}$.

linear combination of these harmonic modes using Fourier analysis. By considering only harmonic solutions, the problem is considerably simplified since it reduces to a series of eigenvalue problems for the spatially varying part of the solutions (eigenfunctions) and the corresponding frequencies (eigenvalues).

In the absence of sources and assuming a monochromatic wave, i.e., with magnetic field $\boldsymbol{H}(\boldsymbol{r},t)=\boldsymbol{H}(\boldsymbol{r})e^{-i\omega t}$, and electric field $\boldsymbol{E}(\boldsymbol{r},t)=\boldsymbol{E}(\boldsymbol{r})e^{-i\omega t}$, Maxwell's equations can be written in the following form:

$$\nabla\times\left(\frac{1}{\varepsilon(\boldsymbol{r})}\nabla\times\boldsymbol{H}(\boldsymbol{r})\right)=\left(\frac{\omega}{c}\right)^2\boldsymbol{H}(\boldsymbol{r}),\quad \text{in } \mathbb{R}^3,$$
$$\frac{1}{\varepsilon(\boldsymbol{r})}\nabla\times(\nabla\times\boldsymbol{E}(\boldsymbol{r}))=\left(\frac{\omega}{c}\right)^2\boldsymbol{E}(\boldsymbol{r}),\quad \text{in } \mathbb{R}^3,$$

where c is the speed of light, and $\varepsilon(\boldsymbol{r})$ is the dielectric function. In two dimensions, there are two possible polarizations of the magnetic and electric fields. In TE (transverse electric) polarization, the electric field is confined to the plane of wave propagation and the magnetic field $\boldsymbol{H}=(0,0,H)$ is perpendicular to this plane. In contrast, in TM (transverse magnetic) polarization, the magnetic field is confined to the plane of wave propagation and the electric field $\boldsymbol{E}=(0,0,E)$ is perpendicular to this plane. In such cases, the Maxwell's equations can be reduced to scalar eigenvalue problems

$$\text{TE}:\quad -\nabla\cdot\left(\frac{1}{\varepsilon(\boldsymbol{r})}\nabla H(\boldsymbol{r})\right)=\left(\frac{\omega}{c}\right)^2H(\boldsymbol{r}),\qquad \text{in } \mathbb{R}^2, \tag{1}$$

$$\text{TM}:\quad -\nabla\cdot(\nabla E(\boldsymbol{r}))=\left(\frac{\omega}{c}\right)^2\varepsilon(\boldsymbol{r})E(\boldsymbol{r}),\qquad \text{in } \mathbb{R}^2\ . \tag{2}$$

Note that the reciprocal of the dielectric function is present in the differential operator for the TE case, whereas the dielectric function is present in the right-hand side for the TM case.

For two-dimensional square lattices the dielectric function satisfies $\varepsilon(\boldsymbol{r})=\varepsilon(\boldsymbol{r}+\boldsymbol{R})$, where $\boldsymbol{R}$ are the crystal lattice vectors.[1] By applying the Bloch–Floquet theory [3,12] for periodic eigenvalue problems we obtain that

$$H(\boldsymbol{r})=e^{i\boldsymbol{k}\cdot\boldsymbol{r}}H_{\boldsymbol{k}}(\boldsymbol{r})\quad\text{and}\quad E(\boldsymbol{r})=e^{i\boldsymbol{k}\cdot\boldsymbol{r}}E_{\boldsymbol{k}}(\boldsymbol{r}),$$

where $H_{\boldsymbol{k}}(\boldsymbol{r})$ and $E_{\boldsymbol{k}}(\boldsymbol{r})$ satisfy

$$\text{TE}:\quad (\nabla+i\boldsymbol{k})\cdot\left(\frac{1}{\varepsilon(\boldsymbol{r})}(\nabla+i\boldsymbol{k})H_{\boldsymbol{k}}(\boldsymbol{r})\right)=\left(\frac{\omega}{c}\right)^2H_{\boldsymbol{k}}(\boldsymbol{r}),\quad \text{in } \Omega, \tag{3}$$

$$\text{TM}:\quad (\nabla+i\boldsymbol{k})\cdot((\nabla+i\boldsymbol{k})E_{\boldsymbol{k}}(\boldsymbol{r}))=\left(\frac{\omega}{c}\right)^2\varepsilon(\boldsymbol{r})E_{\boldsymbol{k}}(\boldsymbol{r}),\quad \text{in } \Omega, \tag{4}$$

respectively. Thus, the effect of considering periodicity is reduced to replacing the indefinite periodic domain by the unit cell Ω and ∇ by $\nabla+i\boldsymbol{k}$ in the original equation, where $\boldsymbol{k}$ is a wave vector in the first Brillouin zone $\mathcal{B}$. Note that the unit cell Ω and the Brillouin zone $\mathcal{B}$ depend on the lattice type (e.g., square or triangular lattices) as well as the crystal lattice vectors $\boldsymbol{R}$. If we further take into consideration the symmetry group of the square lattice [24], we only need to consider all possible wavevectors $\boldsymbol{k}$ on the irreducible Brillouin zone, or (under certain conditions) its boundary [13]. Fig. 1 shows an example of the unit cell and the Brillouin zone for a square lattice.

For notational convenience, we write the above equations in the following operator form:

$$\mathcal{A}u=\lambda\mathcal{M}u,\quad \text{in } \Omega, \tag{5}$$

where, for the TE case, $u\equiv H_{\boldsymbol{k}}(\boldsymbol{r})$, $\lambda\equiv\omega_{\text{TE}}^2/c^2$, and

[1] For a square lattice, $\boldsymbol{R}$ denotes the vectors spanned by $\{a\boldsymbol{e}_1, a\boldsymbol{e}_2\}$, where $\boldsymbol{e}_1$ and $\boldsymbol{e}_2$ are the unit basis vectors and a is the periodicity length of the crystal [13].

$$\mathcal{A}(\varepsilon,\boldsymbol{k}) \equiv -(\nabla + i\boldsymbol{k}) \cdot \left(\frac{1}{\varepsilon(\boldsymbol{r})}(\nabla + i\boldsymbol{k})\right), \qquad \mathcal{M} \equiv I; \tag{6}$$

whereas, for the TM case, $u \equiv E_{\boldsymbol{k}}(\boldsymbol{r}), \lambda \equiv \omega_{\mathrm{TM}}^2/c^2$, and

$$\mathcal{A}(\boldsymbol{k}) \equiv -(\nabla + i\boldsymbol{k}) \cdot (\nabla + i\boldsymbol{k}), \quad \mathcal{M}(\varepsilon) \equiv \varepsilon(\boldsymbol{r})I. \tag{7}$$

Here I denotes the identity operator. We denote by (u^m, λ^m) the mth pair of eigenfunction and eigenvalue of (5) and assume that these eigenpairs are numbered in ascending order: $0 \leqslant \lambda^1 \leqslant \lambda^2 \leqslant \cdots \leqslant \lambda^\infty$.

2.2. The optimization problem

The objective in photonic crystal design is to maximize the bandgap between two consecutive frequency modes. Due to the lack of fundamental length scale in Maxwell's equations, it can be shown that the magnitude of the bandgap scales by a factor of s when the crystal is expanded by a factor of $1/s$. Therefore, it is more meaningful to maximize the *gap–midgap* ratio instead of the absolute bandgap [13]. The gap–midgap ratio between λ^m and λ^{m+1} is defined as

$$J(\varepsilon(\boldsymbol{r})) = \frac{\inf\limits_{\boldsymbol{k}\in\partial\mathcal{B}} \lambda^{m+1}(\varepsilon(\boldsymbol{r}),\boldsymbol{k}) - \sup\limits_{\boldsymbol{k}\in\partial\mathcal{B}} \lambda^{m}(\varepsilon(\boldsymbol{r}),\boldsymbol{k})}{\inf\limits_{\boldsymbol{k}\in\partial\mathcal{B}} \lambda^{m+1}(\varepsilon(\boldsymbol{r}),\boldsymbol{k}) + \sup\limits_{\boldsymbol{k}\in\partial\mathcal{B}} \lambda^{m}(\varepsilon(\boldsymbol{r}),\boldsymbol{k})},$$

where $\partial\mathcal{B}$ represents the irreducible Brillouin zone boundary; see Fig. 1 for example.

A typical characterization of the dielectric function $\varepsilon(\boldsymbol{r})$ is the distribution of two different materials. Suppose that we are given two distinct materials with dielectric constants $\varepsilon_{\min}$ and $\varepsilon_{\max}$ where $\varepsilon_{\min} < \varepsilon_{\max}$. We wish to find arrangements of the materials within the unit cell Ω which result in maximal gap–midgap ratio. To this end, we decompose the unit cell Ω into N_ε disjoint subcells $K_i, 1 \leqslant i \leqslant N_\varepsilon$, such that $\Omega = \cup_{i=1}^{N_\varepsilon} K_i$ and $K_i \cap K_j = \emptyset$ for $i \neq j$. Here we take this subcell grid to be the same as the finite element triangulation of the unit cell as we are going to discretize the continuous eigenvalue problem by the finite element method. Our dielectric function $\varepsilon(\boldsymbol{r})$ takes a unique value between $\varepsilon_{\min}$ and $\varepsilon_{\max}$ on each subcell, namely, $\varepsilon(\boldsymbol{r}) = \varepsilon_i \in \mathbb{R}$ on K_i and $\varepsilon_{\min} \leqslant \varepsilon_i \leqslant \varepsilon_{\max}$. However, due to the symmetry of the square lattice, we only need to define the dielectric function $\varepsilon(\boldsymbol{r})$ over part of the unit cell (1/8 of the unit cell). Hence, in general, the dielectric function $\varepsilon(\boldsymbol{r})$ is discretized into a finite-dimensional vector $\boldsymbol{\varepsilon} = (\varepsilon_1, \ldots, \varepsilon_{n_\varepsilon}) \in \mathbb{R}^{n_\varepsilon}$ (with $n_\epsilon \leqslant N_\epsilon$) which resides in the following admissible region:

$$\mathcal{Q}_{ad} \equiv \{\boldsymbol{\varepsilon} = (\varepsilon_1, \ldots, \varepsilon_{n_\varepsilon}) \in \mathbb{R}^{n_\varepsilon} : \varepsilon_{\min} \leqslant \varepsilon_i \leqslant \varepsilon_{\max}, 1 \leqslant i \leqslant n_\varepsilon\}.$$

This region consists of piecewise-constant functions whose value on every subcell varies between $\varepsilon_{\min}$ and $\varepsilon_{\max}$. Moreover, to render this problem computationally tractable, we replace the irreducible Brillouin zone boundary $\partial\mathcal{B}$ by a finite subset

$$\mathcal{S}_{n_k} = \{\boldsymbol{k}_t \in \partial\mathcal{B}, 1 \leqslant t \leqslant n_k\},$$

where $\boldsymbol{k}_t$, $1 \leqslant t \leqslant n_k$, are wave vectors chosen along the irreducible Brillouin zone boundary. As a result, the bandgap optimization problem that maximizes the gap–midgap ratio between λ^m and λ^{m+1} can be stated as follows:

$$\begin{aligned} &\max_{\boldsymbol{\varepsilon}} J^*(\boldsymbol{\varepsilon}) = \frac{\min_{\boldsymbol{k}\in\mathcal{S}_{n_k}} \lambda^{m+1}(\boldsymbol{\varepsilon},\boldsymbol{k}) - \max_{\boldsymbol{k}\in\mathcal{S}_{n_k}} \lambda^{m}(\boldsymbol{\varepsilon},\boldsymbol{k})}{\min_{\boldsymbol{k}\in\mathcal{S}_{n_k}} \lambda^{m+1}(\varepsilon,\boldsymbol{k}) + \max_{\boldsymbol{k}\in\mathcal{S}_{n_k}} \lambda^{m}(\boldsymbol{\varepsilon},\boldsymbol{k})} \\ &\text{s.t.} \quad \mathcal{A}(\boldsymbol{\varepsilon},\boldsymbol{k})u^j = \lambda^j \mathcal{M}(\boldsymbol{\varepsilon})u^j, \quad j = m, m+1, \ \boldsymbol{k} \in \mathcal{S}_{n_k}, \\ &\qquad \varepsilon_{\min} \leqslant \varepsilon_i \leqslant \varepsilon_{\max}, \qquad 1 \leqslant i \leqslant n_\varepsilon. \end{aligned} \tag{8}$$

In this problem a subtle difference between TE and TM polarizations lies in the operators of the eigenvalue problem: $\mathcal{A}$ and $\mathcal{M}$ take the form of either (6) for the TE case or (7) for the TM case. In either case, note that the eigenvalue problems embedded in (8) must be addressed as part of any computational strategy for the overall solution of (8).

2.3. Discretization of the eigenvalue problem

We consider here the finite element method to discretize the continuous eigenvalue problem (5). This produces the following discrete eigenvalue problem

$$A_h(\boldsymbol{\varepsilon},\boldsymbol{k})u_h^j = \lambda_h^j M_h(\varepsilon)u_h^j, \quad j = 1, \ldots, \mathcal{N}, \quad \boldsymbol{k} \in \mathcal{S}_{n_k}, \tag{9}$$

where $A_h(\boldsymbol{\varepsilon},\boldsymbol{k}) \in \mathbb{C}^{\mathcal{N}\times\mathcal{N}}$ is a Hermitian stiffness matrix and $M_h(\boldsymbol{\varepsilon}) \in \mathbb{R}^{\mathcal{N}\times\mathcal{N}}$ is a symmetric positive definite mass matrix. These matrices are sparse and typically very large ($\mathcal{N} \gg 1$). We consider the approximate eigenvalues in ascending order: $\lambda_h^1 \leqslant \lambda_h^2 \leqslant \ldots \leqslant \lambda_h^{\mathcal{N}}$.

It is important to note that the dependence of the above matrices on the design parameter vector $\boldsymbol{\varepsilon}$ is different for the TE and TM polarizations. In the TE case, A_h^{TE} depends on $\boldsymbol{\varepsilon}$ and M_h^{TE} does not, whereas in the TM case M_h^{TM} depends on $\boldsymbol{\varepsilon}$ and A_h^{TM} does not. More specifically, since $\varepsilon(\boldsymbol{r})$ is a piecewise-constant function on Ω, the $\boldsymbol{\varepsilon}$-dependent matrices can be expressed as

$$A_h^{\mathrm{TE}}(\boldsymbol{\varepsilon},\boldsymbol{k}) = \sum_{i=1}^{n_\varepsilon} \frac{1}{\varepsilon_i} A_{h,i}^{\mathrm{TE}}(\boldsymbol{k}), \quad M_h^{\mathrm{TM}}(\boldsymbol{\varepsilon}) = \sum_{i=1}^{n_\varepsilon} \varepsilon_i M_{h,i}^{\mathrm{TM}}, \tag{10}$$

where the matrices $A_{h,i}^{\mathrm{TE}}(\boldsymbol{k})$ and $M_{h,i}^{\mathrm{TM}}$, $1 \leqslant i \leqslant n_\varepsilon$ are independent of $\boldsymbol{\varepsilon}$. We note that $A_h^{\mathrm{TE}}(\boldsymbol{\varepsilon},\boldsymbol{k})$ is linear with respect to $1/\varepsilon_i$, $1 \leqslant i \leqslant n_\varepsilon$, while $M_h^{\mathrm{TM}}(\boldsymbol{\varepsilon})$ is linear with respect to ε_i, $1 \leqslant i \leqslant n_\varepsilon$. The affine expansion (10) is a direct consequence of the fact that we use piecewise-constant approximation for the dielectric function $\varepsilon(\boldsymbol{r})$. (In the TE case, we will shortly change our decision variables to $y_i = 1/\varepsilon_i$, $1 \leqslant i \leqslant n_\varepsilon$, so as to render A_h^{TE} affine in the variables $y_1, \ldots, y_{n_\varepsilon}$.)

After discretizing the eigenvalue problem (5) by the finite element method, we obtain the following bandgap optimization problem:

$$\begin{aligned} \max_{\boldsymbol{\varepsilon}} \; & J_h(\boldsymbol{\varepsilon}) = \frac{\min_{\boldsymbol{k}\in\mathcal{S}_{n_k}} \lambda_h^{m+1}(\boldsymbol{\varepsilon},\boldsymbol{k}) - \max_{\boldsymbol{k}\in\mathcal{S}_{n_k}} \lambda_h^{m}(\boldsymbol{\varepsilon},\boldsymbol{k})}{\max_{\boldsymbol{k}\in\mathcal{S}_{n_k}} \lambda_h^{m+1}(\boldsymbol{\varepsilon},\boldsymbol{k}) + \max_{\boldsymbol{k}\in\mathcal{S}_{n_k}} \lambda_h^{m}(\boldsymbol{\varepsilon},\boldsymbol{k})} \\ \text{s.t.} \; & A_h(\boldsymbol{\varepsilon},\boldsymbol{k}) u_h^j = \lambda_h^j \mathcal{M}_h(\boldsymbol{\varepsilon}) u_h^j, \quad j = m, m+1, \; \boldsymbol{k} \in \mathcal{S}_{n_k}, \\ & \varepsilon_{\min} \leqslant \varepsilon_i \leqslant \varepsilon_{\max}, \quad 1 \leqslant i \leqslant n_\varepsilon. \end{aligned} \tag{11}$$

Unfortunately, this optimization problem is non-convex; furthermore it suffers from lack of regularity at the optimum. The reason for this is that the eigenvalues λ_h^m and λ_h^{m+1} are typically not smooth functions of $\boldsymbol{\varepsilon}$ at points of multiplicity, and multiple eigenvalues at the optimum are typical of structures with symmetry. As a consequence, the gradient of the objective function $J_h(\boldsymbol{\varepsilon})$ with respect to $\boldsymbol{\varepsilon}$ is not well-defined at points of eigenvalue multiplicity, and thus gradient-based methods often run into serious numerical difficulties and convergence problems.

3. Band structure optimization

In this section we describe our approach to solve the bandgap optimization problem based on a subspace method and semidefinite programming (SDP). In our approach, we first reformulate the original problem as an optimization problem in which we aim to maximize the band gap obtained by restriction of the operator to two orthogonal subspaces. The first subspace consists of eigenfunctions associated to eigenvalues below the bandgap, and the second subspace consists of eigenfunctions whose eigenvalues are above the bandgap. In this way, the eigenvalues are no longer explicitly present in the formulation, and eigenvalue multiplicity no longer leads to lack of regularity. The reformulated optimization problem is exact but non-convex and large-scale. To reduce the problem size, we truncate the high-dimensional subspaces to only a few eigenfunctions below and above the bandgap [5,17], thereby obtaining a new small-scale yet non-convex optimization problem. Finally, we keep the subspaces fixed at a given decision parameter vector to obtain a convex semidefinite optimization problem for which SDP solution methods can be efficiently applied.

3.1. Reformulation of the bandgap optimization problem using subspaces

We first define two additional decision variables:

$$\lambda_h^u := \min_{\boldsymbol{k}\in\mathcal{S}_{n_k}} \lambda_h^{m+1}(\boldsymbol{\varepsilon},\boldsymbol{k}), \quad \lambda_h^\ell := \max_{\boldsymbol{k}\in\mathcal{S}_{n_k}} \lambda_h^{m}(\boldsymbol{\varepsilon},\boldsymbol{k}),$$

and then rewrite the original problem (11) as

$$\begin{aligned} P_0: \max_{\boldsymbol{\varepsilon},\lambda_h^u,\lambda_h^\ell} \; & \frac{\lambda_h^u - \lambda_h^\ell}{\lambda_h^u + \lambda_h^\ell} \\ \text{s.t.} \; & \lambda_h^m(\boldsymbol{\varepsilon},\boldsymbol{k}) \leqslant \lambda_h^\ell, \lambda_h^u \leqslant \lambda_h^{m+1}(\boldsymbol{\varepsilon},\boldsymbol{k}), && \forall \boldsymbol{k} \in \mathcal{S}_{n_k}, \\ & A_h(\boldsymbol{\varepsilon},\boldsymbol{k}) u_h^m = \lambda_h^m M_h(\boldsymbol{\varepsilon}) u_h^m, && \forall \boldsymbol{k} \in \mathcal{S}_{n_k}, \\ & A_h(\boldsymbol{\varepsilon},\boldsymbol{k}) u_h^{m+1} = \lambda_h^{m+1} M_h(\varepsilon) u_h^{m+1}, && \forall \boldsymbol{k} \in \mathcal{S}_{n_k}, \\ & \varepsilon_{\min} \leqslant \varepsilon_i \leqslant \varepsilon_{\max}, && i = 1, \ldots, n_\varepsilon, \\ & \lambda_h^u, \lambda_h^\ell \geqslant 0. \end{aligned} \tag{12}$$

Next, we introduce the following matrices:

$$\Phi^{\varepsilon}(\boldsymbol{k}) := [\Phi_\ell^{\varepsilon}(\boldsymbol{k}) | \Phi_u^{\varepsilon}(\boldsymbol{k})] := [u_h^1(\boldsymbol{\varepsilon},\boldsymbol{k}), \ldots, u_h^m(\varepsilon,\boldsymbol{k}) | u_h^{m+1}(\boldsymbol{\varepsilon},\boldsymbol{k}), \ldots, u_h^{\mathcal{N}}(\boldsymbol{\varepsilon},\boldsymbol{k})],$$

where $\Phi_\ell^{\varepsilon}(\boldsymbol{k})$ and $\Phi_u^{\varepsilon}(\boldsymbol{k})$ consist of the first m eigenvectors and the remaining $\mathcal{N} - m$ eigenvectors, respectively, of the eigenvalue problem:

$$A_h(\boldsymbol{\varepsilon},\boldsymbol{k}) u_h^j = \lambda_h^j M_h(\varepsilon) u_h^j, \quad 1 \leqslant j \leqslant \mathcal{N}.$$

We will also denote the subspaces spanned by the eigenvectors of $\Phi_\ell^{\varepsilon}(\boldsymbol{k})$ and $\Phi_u^{\varepsilon}(\boldsymbol{k})$ as $\mathbf{sp}(\Phi_\ell^{\varepsilon}(\boldsymbol{k}))$ and $\mathbf{sp}(\Phi_u^{\varepsilon}(\boldsymbol{k}))$, respectively.

The first four sets of constraints in (12) can be represented exactly as

$$\Phi_\ell^{\varepsilon *}(\boldsymbol{k})[A_h(\boldsymbol{\varepsilon},\boldsymbol{k}) - \lambda_h^\ell M_h(\boldsymbol{\varepsilon})]\Phi_\ell^{\varepsilon}(\boldsymbol{k}) \preceq 0, \quad \forall \boldsymbol{k} \in \mathcal{S}_{n_k},$$
$$\Phi_u^{\varepsilon *}(\boldsymbol{k})[A_h(\boldsymbol{\varepsilon},\boldsymbol{k}) - \lambda_h^u M_h(\boldsymbol{\varepsilon})]\Phi_u^{\varepsilon}(\boldsymbol{k}) \succeq 0, \quad \forall \boldsymbol{k} \in \mathcal{S}_{n_k},$$

where "$\succeq$" is the Löwner partial ordering on symmetric matrices, i.e., $A \succeq B$ if and only if $A - B$ is positive semidefinite. We therefore obtain the following equivalent optimization problem:

$$\begin{aligned} P_1\colon \max_{\boldsymbol{\varepsilon},\lambda_h^u,\lambda_h^\ell} \ & \frac{\lambda_h^u - \lambda_h^\ell}{\lambda_h^u + \lambda_h^\ell} \\ \text{s.t.} \ & \Phi_\ell^{\varepsilon *}(\boldsymbol{k})[A_h(\varepsilon,\boldsymbol{k}) - \lambda_h^\ell M_h(\boldsymbol{\varepsilon})]\Phi_\ell^{\varepsilon}(\boldsymbol{k}) \preceq 0, && \forall \boldsymbol{k} \in \mathcal{S}_{n_k}, \\ & \Phi_u^{\varepsilon *}(\boldsymbol{k})[A_h(\boldsymbol{\varepsilon},\boldsymbol{k}) - \lambda_h^u M_h(\boldsymbol{\varepsilon})]\Phi_u^{\varepsilon}(\boldsymbol{k}) \succeq 0, && \forall \boldsymbol{k} \in \mathcal{S}_{n_k}, \\ & \varepsilon_{\min} \leqslant \varepsilon_i \leqslant \varepsilon_{\max}, && i = 1,\ldots,n_\varepsilon, \\ & \lambda_h^u, \lambda_h^\ell \geqslant 0. \end{aligned} \tag{13}$$

Although the reformulation P_1 is exact, there is however a subtle difference in the interpretation of P_0 and P_1 : P_0 can be viewed as maximizing the gap–midgap ratio between the two eigenvalues λ_h^m and λ_h^{m+1}; whereas P_1 can be viewed as maximizing the gap–midgap ratio between the two subspaces $\mathbf{sp}(\Phi_\ell^{\varepsilon}(\boldsymbol{k}))$ and $\mathbf{sp}(\Phi_u^{\varepsilon}(\boldsymbol{k}))$. The latter viewpoint allows us to develop an efficient subspace approximation method for solving the bandgap optimization problem as discussed below.

3.2. Subspace approximation and reduction

Let us assume that we are *given* a parameter vector $\hat{\boldsymbol{\varepsilon}}$. We then introduce the associated matrices

$$\Phi^{\hat{\varepsilon}}(\boldsymbol{k}) := [\Phi_\ell^{\hat{\varepsilon}}(\boldsymbol{k})|\Phi_u^{\hat{\varepsilon}}(\boldsymbol{k})] = [u_h^1(\hat{\boldsymbol{\varepsilon}},\boldsymbol{k}),\ldots,u_h^m(\hat{\boldsymbol{\varepsilon}},\boldsymbol{k})|u_h^{m+1}(\hat{\boldsymbol{\varepsilon}},\boldsymbol{k}),\ldots,u_h^{\mathcal{N}}(\hat{\boldsymbol{\varepsilon}},\boldsymbol{k})],$$

where $\Phi_\ell^{\hat{\varepsilon}}(\boldsymbol{k})$ and $\Phi_u^{\hat{\varepsilon}}(\boldsymbol{k})$ consist of the first m eigenvectors and the remaining $\mathcal{N} - m$ eigenvectors, respectively, of the eigenvalue problem

$$A_h(\hat{\boldsymbol{\varepsilon}},\boldsymbol{k})u_h^j = \lambda_h^j M_h(\hat{\boldsymbol{\varepsilon}})u_h^j, \quad 1 \leqslant j \leqslant \mathcal{N}.$$

Under the presumption that $\mathbf{sp}(\Phi_\ell^{\hat{\varepsilon}}(\boldsymbol{k}))$ and $\mathbf{sp}(\Phi_u^{\hat{\varepsilon}}(\boldsymbol{k}))$ are reasonable approximations of $\mathbf{sp}(\Phi_\ell^{\varepsilon}(\boldsymbol{k}))$ and $\mathbf{sp}(\Phi_u^{\varepsilon}(\boldsymbol{k}))$ for $\boldsymbol{\varepsilon}$ near $\hat{\boldsymbol{\varepsilon}}$, we replace $\Phi_\ell^{\varepsilon}(\boldsymbol{k})$ with $\Phi_\ell^{\hat{\varepsilon}}(\boldsymbol{k})$ and $\Phi_u^{\varepsilon}(\boldsymbol{k})$ with $\Phi_u^{\hat{\varepsilon}}(\boldsymbol{k})$ to obtain

$$\begin{aligned} P_2^{\hat{\varepsilon}}\colon \max_{\boldsymbol{\varepsilon},\lambda_h^u,\lambda_h^\ell} \ & \frac{\lambda_h^u - \lambda_h^\ell}{\lambda_h^u + \lambda_h^\ell} \\ \text{s.t.} \ & \Phi_\ell^{\hat{\varepsilon} *}(\boldsymbol{k})[A_h(\boldsymbol{\varepsilon},\boldsymbol{k}) - \lambda_h^\ell M_h(\boldsymbol{\varepsilon})]\Phi_\ell^{\hat{\varepsilon}}(\boldsymbol{k}) \preceq 0, && \forall \boldsymbol{k} \in \mathcal{S}_{n_k}, \\ & \Phi_u^{\hat{\varepsilon} *}(\boldsymbol{k})[A_h(\boldsymbol{\varepsilon},\boldsymbol{k}) - \lambda_h^u M_h(\boldsymbol{\varepsilon})]\Phi_u^{\hat{\varepsilon}}(\boldsymbol{k}) \succeq 0, && \forall \boldsymbol{k} \in \mathcal{S}_{n_k}, \\ & \varepsilon_{\min} \leqslant \varepsilon_i \leqslant \varepsilon_{\max}, && i = 1,\ldots,n_\varepsilon, \\ & \lambda_h^u, \lambda_h^\ell \geqslant 0. \end{aligned} \tag{14}$$

Note in $P_2^{\hat{\varepsilon}}$ that the subspaces $\mathbf{sp}(\Phi_\ell^{\hat{\varepsilon}}(\boldsymbol{k}))$ and $\mathbf{sp}(\Phi_u^{\hat{\varepsilon}}(\boldsymbol{k}))$ are approximations of the subspaces $\mathbf{sp}(\Phi_\ell^{\varepsilon}(\boldsymbol{k}))$ and $\mathbf{sp}(\Phi_u^{\varepsilon}(\boldsymbol{k}))$ and are no longer functions of the decision variable vector $\boldsymbol{\varepsilon}$.

Note also that the semidefinite inclusions in $P_2^{\hat{\varepsilon}}$ are large-scale, i.e., the rank of either the first or second inclusion is at least $\mathcal{N}/2$, for each $\boldsymbol{k} \in \mathcal{S}_{n_k}$, and $\mathcal{N}$ will typically be quite large. In order to reduce the size of the inclusions, we reduce the dimensions of the subspaces by considering only the "important" eigenvectors among $u_h^1(\boldsymbol{\varepsilon},\boldsymbol{k}),\ldots,u_h^m(\boldsymbol{\varepsilon},\boldsymbol{k})$, $u_h^{m+1}(\boldsymbol{\varepsilon},\boldsymbol{k}),\ldots,u_h^{\mathcal{N}}(\boldsymbol{\varepsilon},\boldsymbol{k})$, namely those $a_{\boldsymbol{k}}$ eigenvectors whose eigenvalues lie below but nearest to $\lambda_h^m(\boldsymbol{\varepsilon},\boldsymbol{k})$ and those $b_{\boldsymbol{k}}$ eigenvectors whose eigenvalues lie above but nearest to $\lambda_h^{m+1}(\boldsymbol{\varepsilon},\boldsymbol{k})$, for small values of $a_{\boldsymbol{k}}$, $b_{\boldsymbol{k}}$, typically chosen in the range between 2 and 5, for each $\boldsymbol{k} \in \mathcal{S}_{n_k}$. This yields reduced matrices

$$\Phi_{a_{\boldsymbol{k}}+b_{\boldsymbol{k}}}^{\hat{\varepsilon}}(\boldsymbol{k}) := [\Phi_{a_{\boldsymbol{k}}}^{\hat{\varepsilon}}(\boldsymbol{k})|\Phi_{b_{\boldsymbol{k}}}^{\hat{\varepsilon}}(\boldsymbol{k})] = [u_h^{m-a_{\boldsymbol{k}}+1}(\hat{\boldsymbol{\varepsilon}},\boldsymbol{k}),\ldots,u_h^m(\hat{\boldsymbol{\varepsilon}},\boldsymbol{k})|u_h^{m+1}(\hat{\boldsymbol{\varepsilon}},\boldsymbol{k}),\ldots,u_h^{m+b_{\boldsymbol{k}}}(\hat{\boldsymbol{\varepsilon}},\boldsymbol{k})].$$

Substituting $\Phi_{a_{\boldsymbol{k}}}^{\hat{\varepsilon}}(\boldsymbol{k})$ in place of $\Phi_\ell^{\hat{\varepsilon}*}(\boldsymbol{k})$ and $\Phi_{b_{\boldsymbol{k}}}^{\hat{\varepsilon}}(\boldsymbol{k})$ in place of $\Phi_u^{\hat{\varepsilon}*}(\boldsymbol{k})$ in the formulation $P_2^{\hat{\varepsilon}}$ yields the following reduced optimization formulation:

$$\begin{aligned} P_3^{\hat{\varepsilon}}\colon \max_{\boldsymbol{\varepsilon},\lambda_h^u,\lambda_h^\ell} \ & \frac{\lambda_h^u - \lambda_h^\ell}{\lambda_h^u + \lambda_h^\ell} \\ \text{s.t.} \ & \Phi_{a_{\boldsymbol{k}}}^{\hat{\varepsilon} *}(\boldsymbol{k})[A_h(\boldsymbol{\varepsilon},\boldsymbol{k}) - \lambda_h^\ell M_h(\boldsymbol{\varepsilon})]\Phi_{a_{\boldsymbol{k}}}^{\hat{\varepsilon}}(\boldsymbol{k}) \preceq 0, && \forall \boldsymbol{k} \in \mathcal{S}_{n_k}, \\ & \Phi_{b_{\boldsymbol{k}}}^{\hat{\varepsilon} *}(\boldsymbol{k})[A_h(\boldsymbol{\varepsilon},\boldsymbol{k}) - \lambda_h^u M_h(\boldsymbol{\varepsilon})]\Phi_{b_{\boldsymbol{k}}}^{\hat{\varepsilon}}(\boldsymbol{k}) \succeq 0, && \forall \boldsymbol{k} \in \mathcal{S}_{n_k}, \\ & \varepsilon_{\min} \leqslant \varepsilon_i \leqslant \varepsilon_{\max}, && i = 1,\ldots,n_\varepsilon, \\ & \lambda_h^u, \lambda_h^\ell \geqslant 0. \end{aligned} \tag{15}$$

In this way the formulation $P_3^{\hat{\varepsilon}}$ seeks to model only the anticipated "active" eigenvalue constraints, in exact extension of active-set methods in nonlinear optimization. The integers $a_{\boldsymbol{k}}$, $b_{\boldsymbol{k}}$ are determined indirectly through user-defined parameters $r_l > 0$, and $r_u > 0$, where we retain only those eigenvectors whose eigenvalues are within $100r_l\%$ beneath $\lambda_h^m(\hat{\boldsymbol{\varepsilon}}, \boldsymbol{k})$ or whose eigenvalues are within $100r_u\%$ above $\lambda_h^{m+1}(\hat{\boldsymbol{\varepsilon}}, \boldsymbol{k})$. This translates to choosing $a_{\boldsymbol{k}}, b_{\boldsymbol{k}} \in \mathbb{N}_+$ as the smallest integers that satisfy

$$\frac{\lambda_h^m(\hat{\boldsymbol{\varepsilon}}, \boldsymbol{k}) - \lambda_h^{m-a_{\boldsymbol{k}}+1}(\hat{\boldsymbol{\varepsilon}}, \boldsymbol{k})}{\lambda_h^m(\hat{\boldsymbol{\varepsilon}}, \boldsymbol{k})} \leqslant r_l \leqslant \frac{\lambda_h^m(\hat{\boldsymbol{\varepsilon}}, \boldsymbol{k}) - \lambda_h^{m-a_{\boldsymbol{k}}}(\hat{\boldsymbol{\varepsilon}}, \boldsymbol{k})}{\lambda_h^m(\hat{\boldsymbol{\varepsilon}}, \boldsymbol{k})},$$
$$\frac{\lambda_h^{m+b_{\boldsymbol{k}}}(\hat{\boldsymbol{\varepsilon}}, \boldsymbol{k}) - \lambda_h^{m+1}(\hat{\boldsymbol{\varepsilon}}, \boldsymbol{k})}{\lambda_h^{m+1}(\hat{\boldsymbol{\varepsilon}}, \boldsymbol{k})} \leqslant r_u \leqslant \frac{\lambda_h^{m+b_{\boldsymbol{k}}+1}(\hat{\boldsymbol{\varepsilon}}, \boldsymbol{k}) - \lambda_h^{m+1}(\hat{\boldsymbol{\varepsilon}}, \boldsymbol{k})}{\lambda_h^{m+1}(\hat{\boldsymbol{\varepsilon}}, \boldsymbol{k})}.$$

The dimensions of the resulting subspaces $\mathbf{sp}(\Phi_{a_{\boldsymbol{k}}}^{\hat{\varepsilon}}(\boldsymbol{k}))$ and $\mathbf{sp}(\Phi_{b_{\boldsymbol{k}}}^{\hat{\varepsilon}}(\boldsymbol{k}))$ are typically very small ($a_{\boldsymbol{k}}, b_{\boldsymbol{k}} \sim 2, \ldots, 5$). Furthermore, the subspaces are well-spanned by including all relevant eigenvectors corresponding to those eigenvalues with multiplicity at or near the current min/max values.

We observe that $P_3^{\hat{\varepsilon}}$ has significantly smaller semidefinite inclusions than if the *full* subspaces were used. Also, the subspaces are kept *fixed* at $\hat{\boldsymbol{\varepsilon}}$ in order to reduce the nonlinearity of the underlying problem. Furthermore, we show below that for the TE and TM polarizations that $P_3^{\hat{\varepsilon}}$ can be easily re-formulated as a linear fractional semidefinite program, and hence is solvable using modern interior-point methods.

3.3. Fractional SDP Formulations for TE and TM Polarizations

We now show that by a simple change of variables for each of the TE and TM polarizations, problem $P_3^{\hat{\varepsilon}}$ can be converted to a linear fractional semidefinite program and hence can be further converted to a linear semidefinite program.

3.3.1. TE polarization

We introduce the following new decision variable notation for convenience:

$$\boldsymbol{y} := (y_1, y_2, \ldots, y_{n_y}) := (1/\varepsilon_1, \ldots, 1/\varepsilon_{n_\varepsilon}, \lambda_h^\ell, \lambda_h^u),$$

and set $y_{\min} = 1/\varepsilon_{\max}$ and $y_{\max} = 1/\varepsilon_{\min}$. We also amend our notation to write various functional dependencies on $\boldsymbol{y}$ instead of $\boldsymbol{\varepsilon}$ such as $\Phi_\ell^{\hat{\boldsymbol{y}}}(\boldsymbol{k})$. Utilizing (10), we re-write $P_3^{\hat{\varepsilon}}$ for the TE polarization as

$$\begin{aligned}
P_{\mathrm{TE}}^{\hat{\boldsymbol{y}}}\text{:}\quad & \max_{\boldsymbol{y}} \ \frac{y_{n_y} - y_{n_y-1}}{y_{n_y} + y_{n_y-1}} \\
\text{s.t.}\quad & \Phi_{a_{\boldsymbol{k}}}^{\hat{\boldsymbol{y}}*}(\boldsymbol{k}) \left[\sum_{i=1}^{n_y-2} y_i A_{h,i}^{\mathrm{TE}}(\boldsymbol{k}) - y_{n_y-1} M_h^{\mathrm{TE}} \right] \Phi_{a_{\boldsymbol{k}}}^{\hat{\boldsymbol{y}}}(\boldsymbol{k}) \preceq 0, \quad \forall \boldsymbol{k} \in \mathcal{S}_{n_k}, \\
& \Phi_{b_{\boldsymbol{k}}}^{\hat{\boldsymbol{y}}*}(\boldsymbol{k}) \left[\sum_{i=1}^{n_y-2} y_i A_{h,i}^{\mathrm{TE}}(\boldsymbol{k}) - y_{n_y} M_h^{\mathrm{TE}} \right] \Phi_{b_{\boldsymbol{k}}}^{\hat{\boldsymbol{y}}}(\boldsymbol{k}) \succeq 0, \quad \forall \boldsymbol{k} \in \mathcal{S}_{n_k}, \\
& y_{\min} \leqslant y_i \leqslant y_{\max}, \qquad i = 1, \ldots, n_y - 2, \\
& y_{n_y-1} \ , \ y_{n_y} \geqslant 0.
\end{aligned} \tag{16}$$

We note that the objective function is a linear fractional expression and the constraint functions are linear functions of the variables $\boldsymbol{y}$. Therefore $P_{\mathrm{TE}}^{\hat{\boldsymbol{y}}}$ is a linear fractional SDP. Using a standard homogenization [6,8], a linear fractional SDP can be converted to a linear SDP.[2]

3.3.2. TM polarization

We introduce slightly different decision variable notation for convenience:

$$\boldsymbol{z} := (z_1, z_2, \ldots, z_{n_z}) := (\varepsilon_1, \ldots, \varepsilon_{n_\varepsilon}, 1/\lambda_h^\ell, 1/\lambda_h^u),$$

and set $z_{\min} = \varepsilon_{\min}$ and $z_{\max} = \varepsilon_{\max}$. Similar to the TE case, we amend our notation to write various functional dependencies on $\boldsymbol{z}$ instead of $\boldsymbol{\varepsilon}$ such as $\Phi_\ell^{\hat{\boldsymbol{z}}}(\boldsymbol{k})$. Noting that

$$\frac{\lambda_h^u - \lambda_h^\ell}{\lambda_h^u + \lambda_h^\ell} = \frac{z_{n_z-1} - z_{n_z}}{z_{n_z-1} + z_{n_z}},$$

utilizing (10), and multiplying the semidefinite inclusions of (15) by z_{n_z-1} and z_{n_z}, respectively, we re-write $P_3^{\hat{\varepsilon}}$ for the TM polarization as

[2] Indeed, for notational simplicity consider a linear fractional optimization problem of the form $\max_x \frac{c^T x}{d^T x}$ subject to $b - Ax \in K_1, x \in K_2$, where $d^T x > 0$ for all feasible x and K_1, K_2 are convex cones. Then this problem is equivalent to the problem $\max_{w,\theta} c^T w$ subject to $b\theta - Aw \in K_1, w \in K_2, d^T w = 1, \theta \geqslant 0$, under the elementary transformations $x \leftarrow (w/\theta)$ and $(w, \theta) \leftarrow (x/d^T x, 1/d^T x)$, see [6,8].

$$
\begin{aligned}
P_{\mathrm{TM}}^{\hat{\boldsymbol{z}}}: \quad & \max_{\boldsymbol{z}} \quad \frac{z_{n_z-1}-z_{n_z}}{z_{n_z-1}+z_{n_z}} \\
\text{s.t.} \quad & \Phi_{a_{\boldsymbol{k}}}^{\hat{\boldsymbol{z}}*}(\boldsymbol{k})\left[z_{n_z-1}A_h^{\mathrm{TM}}(\boldsymbol{k})-\sum_{i=1}^{n_z-2} z_i M_{h,i}^{\mathrm{TM}}\right]\Phi_{a_{\boldsymbol{k}}}^{\hat{\boldsymbol{z}}}(\boldsymbol{k}) \preceq 0, \quad \forall \boldsymbol{k}\in\mathcal{S}_{n_k}, \\
& \Phi_{b_{\boldsymbol{k}}}^{\hat{\boldsymbol{z}}*}(\boldsymbol{k})\left[z_{n_z}A_h^{\mathrm{TM}}(\boldsymbol{k})-\sum_{i=1}^{n_z-2} z_i M_{h,i}^{\mathrm{TM}}\right]\Phi_{b_{\boldsymbol{k}}}^{\hat{\boldsymbol{z}}}(\boldsymbol{k}) \succeq 0, \quad \forall \boldsymbol{k}\in\mathcal{S}_{n_k}, \\
& z_{\min} \leqslant z_i \leqslant z_{\max}, \qquad\qquad i=1,\ldots,n_z-2, \\
& z_{n_z-1},\ z_{n_z} \geqslant 0.
\end{aligned} \tag{17}
$$

Here again the objective function is a linear fractional form and the constraint functions are linear functions of the variables $\boldsymbol{z}$. Therefore $P_{\mathrm{TM}}^{\hat{\boldsymbol{z}}}$ is a linear fractional SDP with format similar to that of $P_{\mathrm{TE}}^{\hat{\boldsymbol{y}}}$.

Since both $P_{\mathrm{TE}}^{\hat{\boldsymbol{y}}}$ and $P_{\mathrm{TM}}^{\hat{\boldsymbol{z}}}$ are linear fractional semidefinite programs, they can be solved very efficiently by using modern interior point methods. Here we use the SDPT3 software [22] for this task.

3.4. Main algorithm

We summarize our numerical approach for solving the bandgap optimization problem of the TE polarization in the following Table 1. Essentially the same algorithm (with the modifications described in the previous section) is used to solve the bandgap optimization problem of the TM polarization.

4. Results and discussion

4.1. Model setup

We consider a two-dimensional photonic crystal confined in the computational domain of a unit cell of the square lattice, and with square domain $\Omega \equiv [-1,1]\times[-1,1]$. The domain Ω is decomposed into a uniform quadrilateral (in particular, we use square elements for the square lattice) grid of dimensions 64×64, which yields a mesh size of $h = 1/32$ and 4096 linear square elements.

The dielectric function $\boldsymbol{\varepsilon}$ is composed of two materials with dielectric constants $\varepsilon_{\min} = 1$ (air) and $\varepsilon_{\max} = 11.4$ (GaAs). As mentioned earlier in Section 2.2, the symmetry of the lattice can be exploited to further reduce the dielectric function to be defined in only 1/8 of the computation domain. The number of decision variables relating the dielectric material $(\varepsilon_i,\ i=1,2,\ldots,n_\varepsilon)$ is thus reduced to $n_\varepsilon = (1+32)\times 32/2 = 528$. Fig. 2 shows an illustration of a coarse mesh (16×16) and dielectric function for the square lattice to aid visualization; note that the actual computational mesh (64×64) is finer than this one. The shaded cells represent those modeled by ε, and the rest are obtained through symmetry. Furthermore, in this case, the irreducible Brillouin zone $\mathcal{B}$ is the triangle shown in Fig. 1, with $n_k = 12$ $\boldsymbol{k}$-points taken along the boundary of this region $(\partial\mathcal{B})$. Band diagrams plotted in the figures below show the eigenvalues moving along the boundary of $\mathcal{B}$, from Γ to X to M and back to Γ.

4.2. Choices of parameters

4.2.1. Initial configuration

Because the underlying optimization problem may have many local optima, the performance of our method can be sensitive to the choice of the initial values of the decision variables $\boldsymbol{y}^0$ (or $\boldsymbol{z}^0$), which in turn depend on the initial configuration $\boldsymbol{\varepsilon}^0$. Indeed, different initial configurations do lead to different local optima as shown in Fig. 3 for the second TE bandgap and

Table 1
Main algorithm for solving the bandgap optimization problem.

Implementation steps
Step 1. Start with an initial guess $\boldsymbol{y}^0$ and an error tolerance ϵ_{tol}, and set $\hat{\boldsymbol{y}} := \boldsymbol{y}^0$.
Step 2. For each wave vector $\boldsymbol{k}\in\mathcal{S}_{n_k}$, do:
Determine the subspace dimensions $a_{\boldsymbol{k}}$ and $b_{\boldsymbol{k}}$.
Compute the matrices $\Phi_{a_{\boldsymbol{k}}}^{\hat{\boldsymbol{y}}}(\boldsymbol{k})$ and $\Phi_{b_{\boldsymbol{k}}}^{\hat{\boldsymbol{y}}}(\boldsymbol{k})$.
Step 3. Form the semidefinite program $P_{\mathrm{TE}}^{\hat{\boldsymbol{y}}}$.
Step 4. Solve $P_{\mathrm{TE}}^{\hat{\boldsymbol{y}}}$ for an optimal solution $\boldsymbol{y}^*$.
Step 5. If $\|\boldsymbol{y}^*-\hat{\boldsymbol{y}}\| \leqslant \epsilon_{\mathrm{tol}}$, stop and return the optimal solution $\boldsymbol{y}^*$.
Else update $\hat{\boldsymbol{y}} \leftarrow \boldsymbol{y}^*$ and go to **Step 2**.

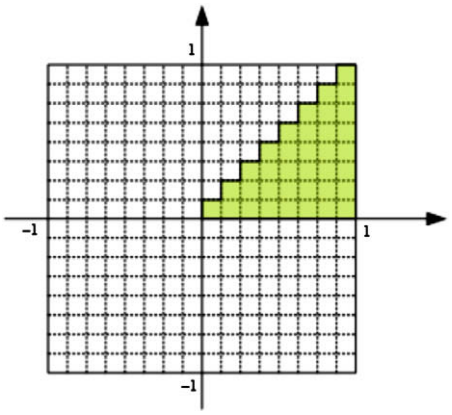

Fig. 2. An illustration of a coarse mesh (16×16) and dielectric function for the square lattice. The shaded cells indicate the decision variables relating the dielectric material ($\varepsilon_i,\ i = 1, 2, \ldots, n_\varepsilon$). Note that the actual computational mesh (64×64) is finer than this one.

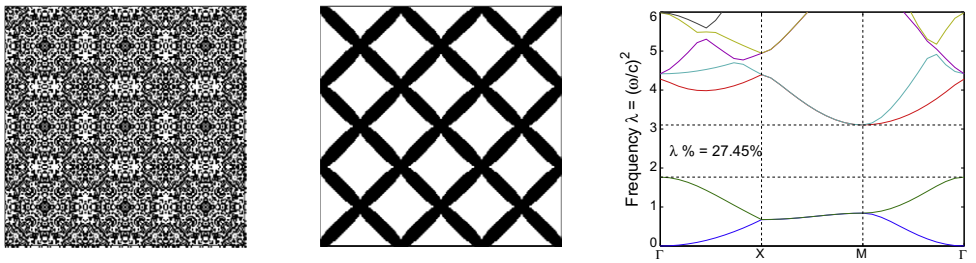

(a) Initial crystal configuration #1 (b) Optimized crystal structure #1 (c) Optimized band structure #1

(d) Initial crystal configuration #2 (e) Optimized crystal structure #2 (f) Optimized band structure #2

Fig. 3. Two locally optimal bandgaps between λ^2_{TE} and λ^3_{TE} in the square lattice.

in Fig. 4 for the fourth TM bandgap. Therefore, the choice of the initial configuration is important. We examine here two different types of initial configurations: photonic crystals exhibiting bandgaps at the low frequency spectrum and random distribution.

The well-known photonic crystals (e.g., dielectric rods in air – Fig. 4(a), air holes in dielectric material, orthogonal dielectric veins – Fig. 3(d)) exhibit band-gap structures at the low frequency spectrum. Such a distribution seems to be a sensible choice for the initial configuration as it resembles various known optimal structures [4]. When these well-known photonic crystals are used as the initial configuration, our method easily produces the bandgap structures at the low frequency mode (typically, the first three TE and TM modes). On the other hand, maximizing the bandgap at the high frequency mode (typically, above the first three TE and TM modes) tends to produce more complicated structures which are very different from the known photonic crystals mentioned above. As a result, when these photonic crystals are used as the initial configurations for maximizing the bandgap at the high frequency mode, the obtained results are less satisfactory.

Random initial configurations such as Fig. 3(a) and (d) have very high spatial variation and may thus be suitable for maximizing the bandgap at the high frequency mode. Indeed, we observe that random distributions often yield larger bandgaps (better results) than the known photonic crystals for the high frequency modes. Of course, the random initialization does not eliminate the possibility of multiple local optima intrinsic to the physical problem. In view of this effect, we use multiple

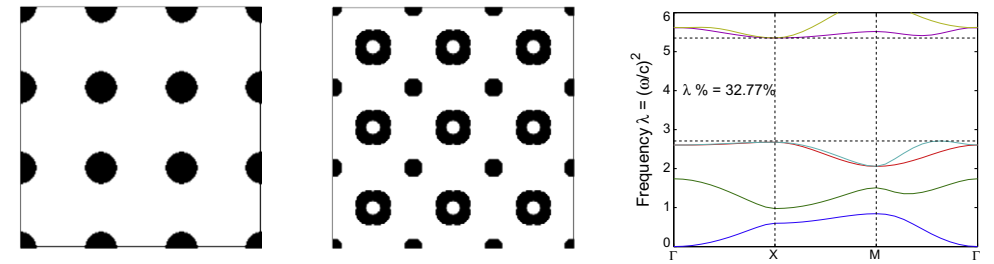

(a) Initial crystal configuration #1 (b) Optimized crystal structure #1 (c) Optimized band structure #1

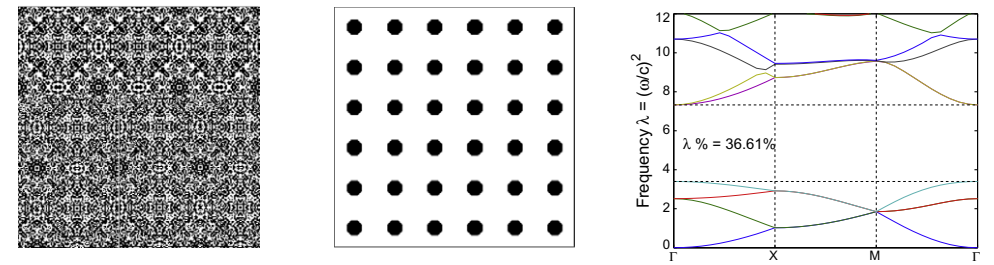

(d) Initial crystal configuration #2 (e) Optimized crystal structure #2 (f) Optimized band structure #2

Fig. 4. Two locally optimal bandgaps between λ^4_{TM} and λ^5_{TM} in the square lattice.

random distributions to initialize our method. In particular, we start our main algorithm with a number of *uniformly* random distributions as initial configurations to obtain the optimal structures in our numerical results discussed below.

4.2.2. Subspace dimensions

The dimensions of the subspaces $\mathbf{sp}(\Phi^{\hat{y}}_{a_{\boldsymbol{k}}}(\boldsymbol{k}))$ and $\mathbf{sp}(\Phi^{\hat{y}}_{b_{\boldsymbol{k}}}(\boldsymbol{k}))$ (or $\mathbf{sp}(\Phi^{\hat{z}}_{a_{\boldsymbol{k}}})$ and $\mathbf{sp}(\Phi^{\hat{z}}_{b_{\boldsymbol{k}}})$) are determined indirectly by the parameters r_l and r_u. A good choice of r_l (and r_u) is one that returns $a_{\boldsymbol{k}} \ll \mathcal{N}$ (and $b_{\boldsymbol{k}} \ll \mathcal{N}$), and at the same time includes the "important" eigenvectors to enhance convergence to an optimum. In our numerical experiments, we choose $r_u = r_l = 0.1$ which in turn leads to the resulting subspace dimensions $a_{\boldsymbol{k}}$ and $b_{\boldsymbol{k}}$ in the range of $[2, 5]$. Moreover, we find that choosing larger values of r_u and r_l (e.g., $r_l = r_u = 0.2$), which in turn increases $a_{\boldsymbol{k}}$ and $b_{\boldsymbol{k}}$ and hence increases computational cost, does not yield fewer iterations than choosing $r_u = r_l = 0.1$.

4.3. Computational cost

All the computations have been carried out using MATLAB and run on a Linux PC with processor Intel Xeon E5550, 2.67 GHz. One run of the algorithm typically takes 0.5–10.0 min, which includes 4–30 outer iterations; each iteration consists of one pass of Steps 2–5 of the main algorithm in Table 1.

Due to the presence of local maxima as well our use of randomly chosen starting point configurations, the times as well as the quality of the resulting solution can vary. For this reason, we make 10 runs of our algorithm corresponding to 10 randomly chosen starting point configurations, and report our aggregate results in Table 2. The table shows average execution times and average number of outer iterations for each case. Since our method and the choice of initial configurations do not guarantee that the solutions will have a positive bandgap, we also report the number of successful runs, where a run is judged to be successful if the resulting gap–midgap ratio is at least 10%.

Table 2
Average computation time, average number of outer iterations, and total number of successes of 10 runs for optimizing various band gaps, for both TE and TM polarization. Here $\Delta\lambda^{TE}_{i,i+1}$ denotes the gap–midgap ratio between the ith and $(i+1)$th eigenvalue for the TE polarization.

	$\Delta\lambda^{\mathrm{TE}}_{1,2}$	$\Delta\lambda^{\mathrm{TE}}_{2,3}$	$\Delta\lambda^{\mathrm{TE}}_{3,4}$	$\Delta\lambda^{\mathrm{TE}}_{4,5}$	$\Delta\lambda^{\mathrm{TE}}_{5,6}$	$\Delta\lambda^{\mathrm{TE}}_{6,7}$	$\Delta\lambda^{\mathrm{TE}}_{7,8}$	$\Delta\lambda^{\mathrm{TE}}_{8,9}$	$\Delta\lambda^{\mathrm{TE}}_{9,10}$
Average execution time (min)	1.3	1.4	2.4	1.7	2.9	3.2	3.0	3.4	5.1
Average outer iterations	9.0	9.0	14.1	7.7	14.1	15.5	13.0	14.2	23.5
Successes (out of 10 runs)	7	6	4	3	5	1	7	2	1
Average execution time (min)	0.42	0.72	0.81	1.6	1.7	2.2	2.3	2.2	4.6
Average outer iterations	3.4	4.1	5.0	8.4	8.9	11.7	11.0	10.9	22.5
Successes (out of 10 runs)	10	8	6	2	9	7	3	3	2

Table 2 shows that in general TM problems usually solve faster and require fewer outer iterations than TE problems. This observation is consistent with the result reported in [15], and is possibly caused by higher non-convexity of the original TE optimization problem. Table 2 also shows that lower eigenvalue bandgap optimization problems tend to require less computation time, and yields wider bandgaps more consistently. To explore this further, we also performed 30 runs with random initial conditions for two representative bandgap cases (the second and the ninth bands), and report histograms of the gap–midgap ratios for these runs in Fig. 5. For the second bandgap, the histograms show that 53.3% and 90% of the cases are successful for the TE and the TM problems, respectively. For the ninth bandgap the numbers are substantially lower, namely 13.3% and 16.7%, respectively.

Table 3 shows the progressive increase in computation cost as the mesh is refined, using the $\Delta\lambda_{2,3}$ problem as an illustrative example. Here the total computation cost is decomposed into solving the eigenvalue problem, solving the SDP problem, and the remaining cost. We observe that the computation time increases rapidly as we refine the mesh and that the computation time is dominated by the time to solve the SDP problem. This is because the number of decision variables increases

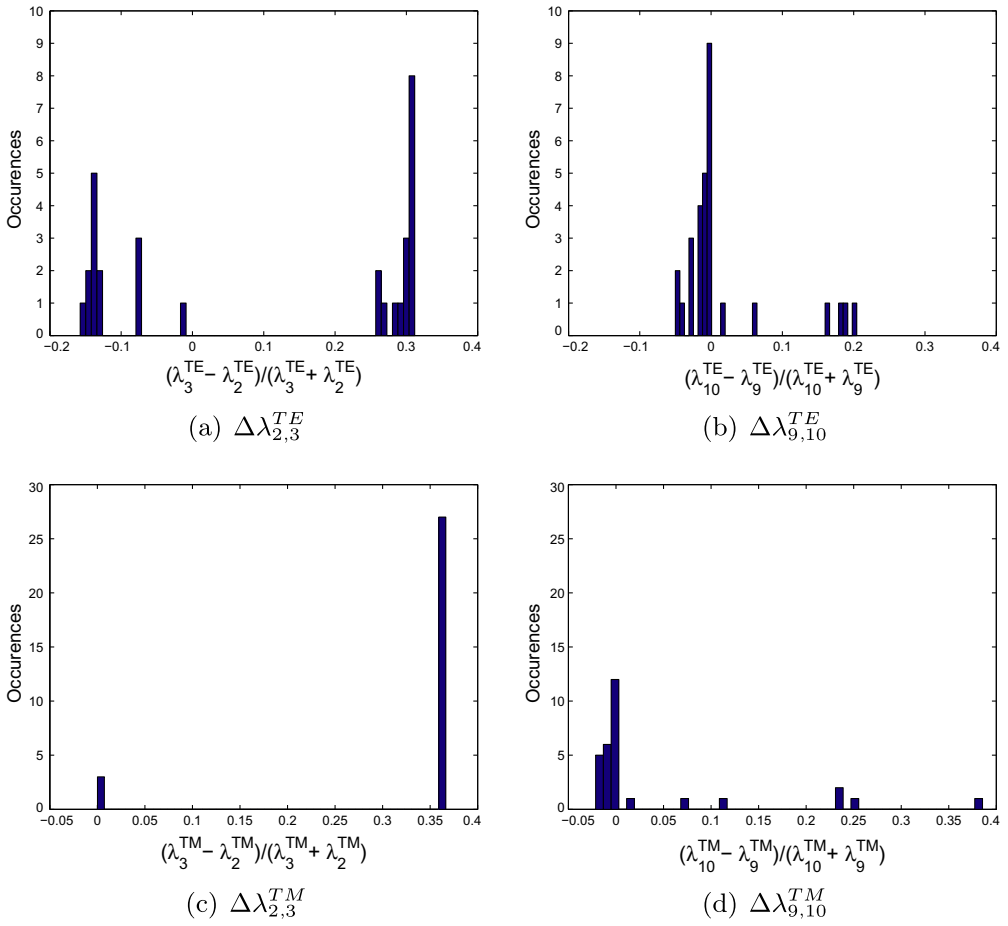

Fig. 5. Histograms of gap–midgap ratios for 30 runs with random initial configurations, for the second and ninth bands.

Table 3
Average computation cost (and the breakdown) of 10 runs as the mesh is refined.

$\Delta\lambda_{2,3}$	TE				TM			
Mesh size	16×16	32×32	64×64	128×128	16×16	32×32	64×64	128×128
Eigenvalue solve	22.1%	21.3%	19.5%	4.9%	22.3%	22.0%	18.5%	5.9%
SDP solve	56.4%	57.1%	61.5%	78.4%	57.3%	60.9%	65.1%	78.3%
Other cost	21.5%	21.6%	19.0%	16.7%	20.4%	17.1%	16.4%	15.8%
Total time (min)	0.15	0.32	1.4	23.7	0.08	0.15	0.72	10.0
Outer iterations	6.5	8.1	9.0	9.0	4.0	4.5	4.1	4.5

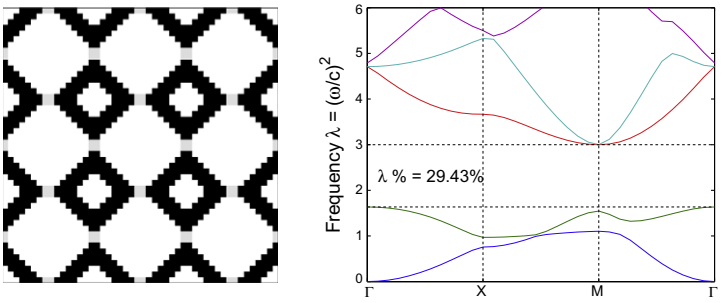

(a) Optimized crystal structure (b) Optimized band structure

Fig. 6. Optimal band between λ^2_{TE} and λ^3_{TE} of mesh size 16×16.

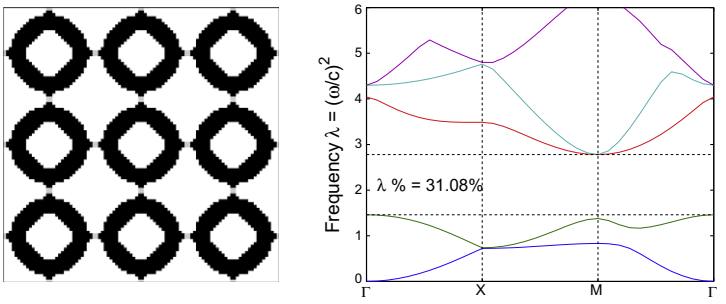

(a) Optimized crystal structure (b) Optimized band structure

Fig. 7. Optimal band between λ^2_{TE} and λ^3_{TE} of mesh size 32×32.

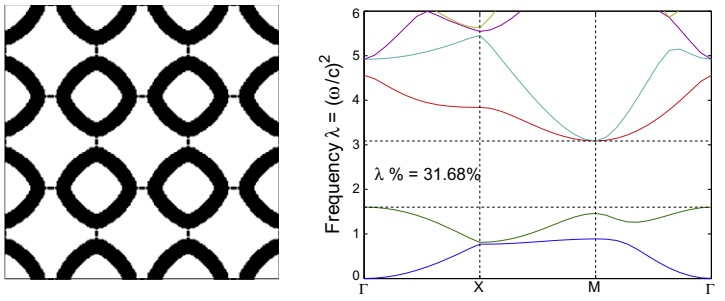

(a) Optimized crystal structure (b) Optimized band structure

Fig. 8. Optimal band between λ^2_{TE} and λ^3_{TE} of mesh size 64×64.

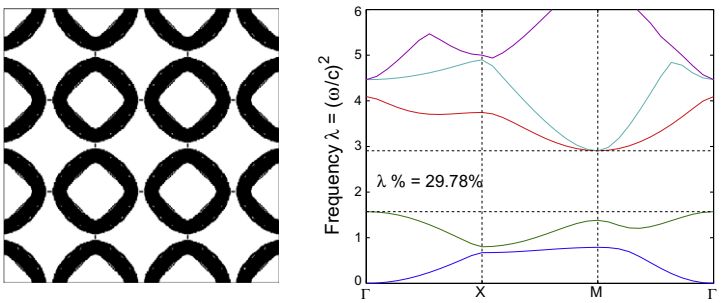

(a) Optimized crystal structure (b) Optimized band structure

Fig. 9. Optimal band between λ^2_{TE} and λ^3_{TE} of mesh size 128×128.

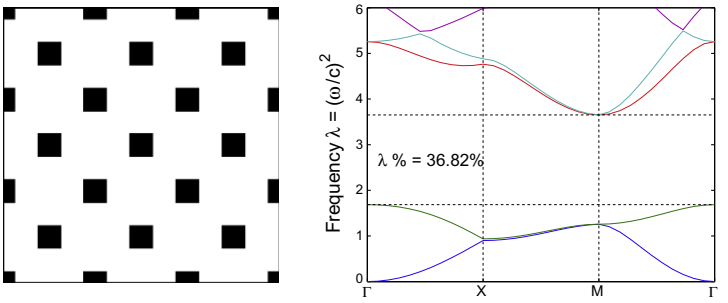

(a) Optimized crystal structure (b) Optimized band structure

Fig. 10. Optimal band between λ^2_{TM} and λ^3_{TM} of mesh size 16×16.

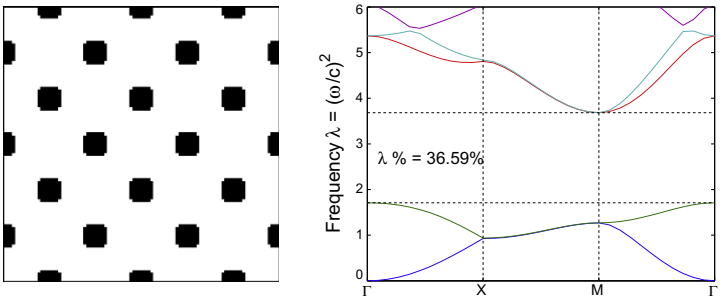

(a) Optimized crystal structure (b) Optimized band structure

Fig. 11. Optimal band between λ^2_{TM} and λ^3_{TM} of mesh size 32×32.

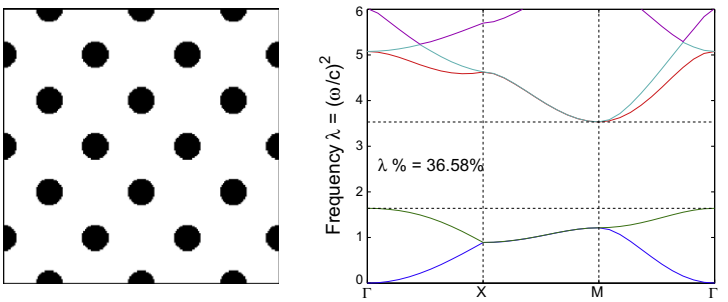

(a) Optimized crystal structure (b) Optimized band structure

Fig. 12. Optimal band between λ^2_{TM} and λ^3_{TM} of mesh size 64×64.

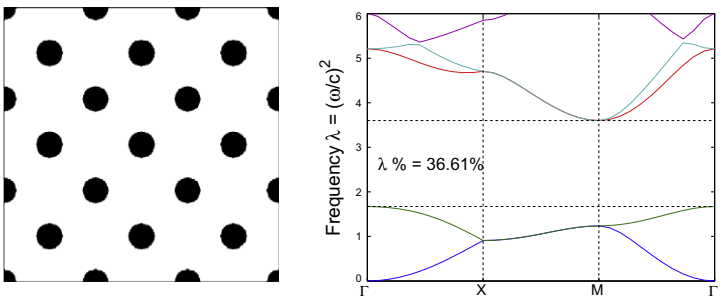

(a) Optimized crystal structure (b) Optimized band structure

Fig. 13. Optimal band between λ^2_{TM} and λ^3_{TM} of mesh size 128×128.

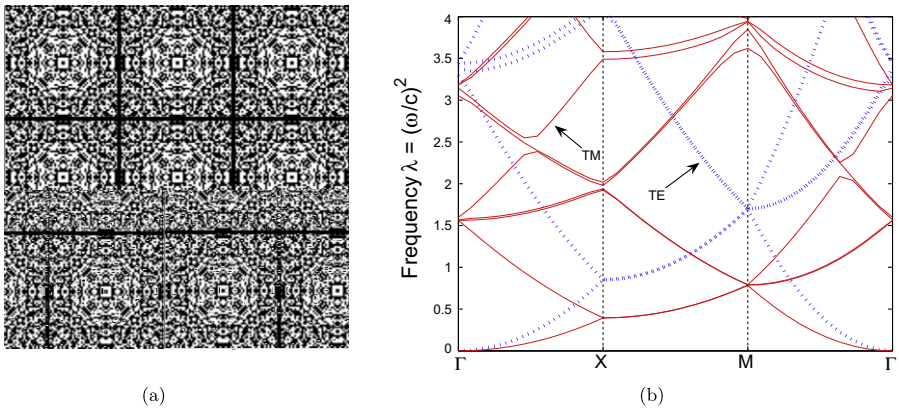

Fig. 14. (a) Random starting structure with translation, rotation, and reflection symmetry, 3×3 unit cells in square lattice. (b) Band structure before optimization.

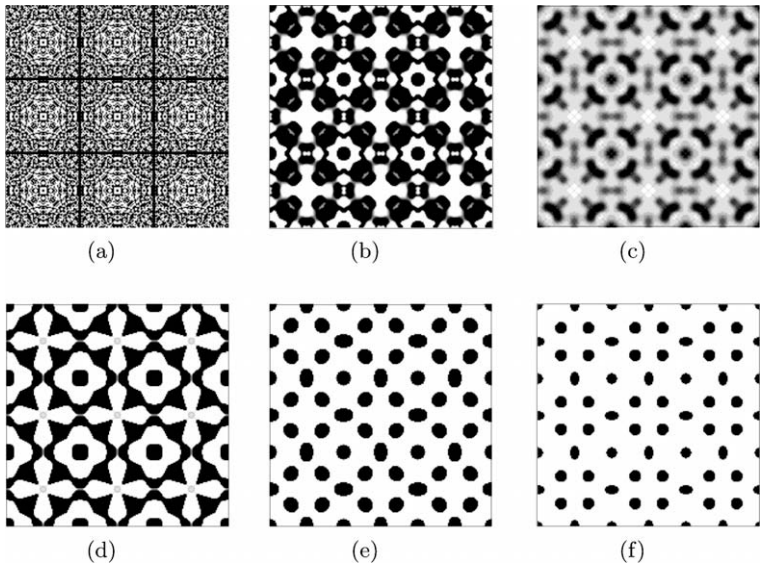

Fig. 15. The evolution of the square lattice crystal structure for optimizing the gap–midgap ratio between λ_{TM}^{7} and λ_{TM}^{8}.

by a factor of four after each mesh refinement, due to the fact that uniform mesh refinement increases the number of elements by a factor of four as the mesh size is halved.

The optimized crystal and band structures for four different meshes are shown in Figs. 6–16. We see that the optimized crystal structures of coarser meshes topologically resemble those of finer meshes and that their gap–midgap ratios are quite close to each other. This seems to indicate that adaptive mesh refinement strategies may be effective for computing these structures.

Before ending this subsection, we discuss possible ways to improve the computation cost of our procedure, while capturing the micro features of the optimized photonic crystals. The above insight on mesh size refinement points to potentially large saving from using mesh adaptivity and incorporating a non-uniform grid for the representation of the dielectric function, as well as the eigenvalue calculation. This approach may reduce the number of decision variables considerably and thus result in significant computational savings. Further computational savings may result from improving our current strategy for choosing the initial configuration (namely, randomization). One strategy that will be considered is to modify the randomization approach to include positive correlation for adjacent cells.

4.4. Optimal structures

We start the optimization procedure with a random distribution of the dielectric, such as the one shown in Fig. 14(a). The corresponding band structures of the TE and TM fields are shown in Fig. 14(b). In Fig. 15, we present an example of the evo-

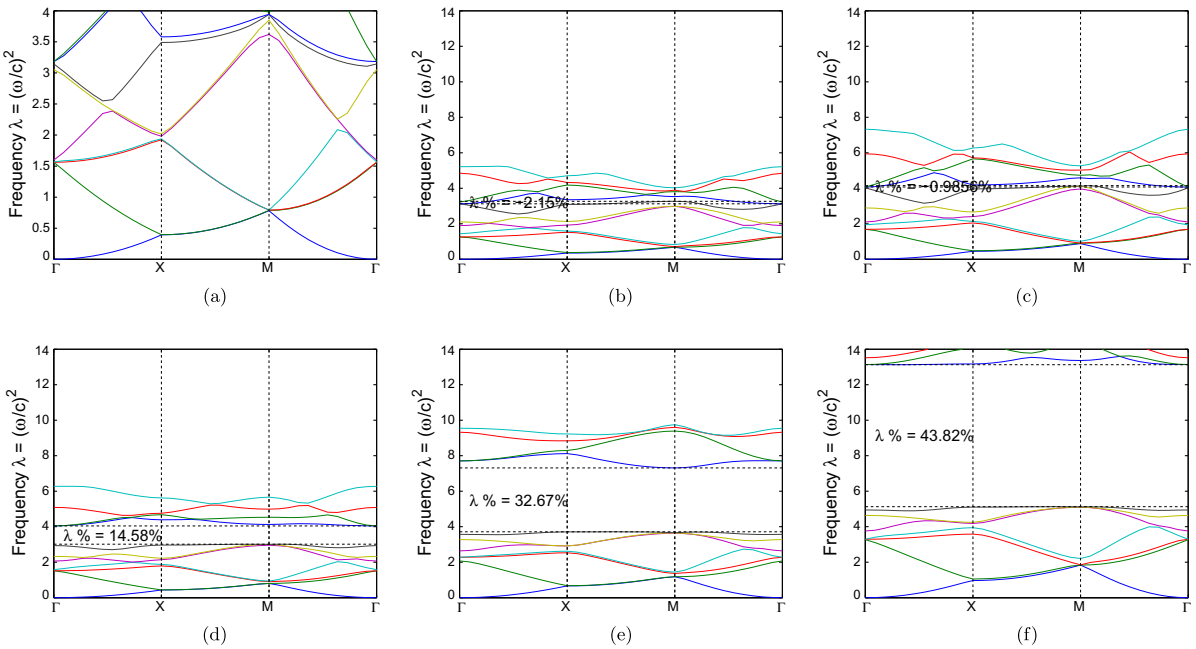

Fig. 16. The corresponding band structure (of Fig. 15) and the gap–midgap ratio between $\lambda^{7}_{\mathrm{TM}}$ and $\lambda^{8}_{\mathrm{TM}}$ in the square lattice.

lution of the crystal structure as the optimization process progresses. (The light color indicates the low dielectric constant and the dark color denotes the high dielectric constant.) As illustrated in Fig. 16, the gap–midgap ratio starts from a negative value (−8.93%) corresponding to the random configuration (Fig. 16(a)) and increases up to +43.82% corresponding to the optimal configuration (Fig. 16(f)) at which time the optimization process terminates successfully. Another example of the optimization evolution for TE polarization is shown in Figs. 17 and 18, in which the gap–midgap ratio increases from −39.21% to +29.23%.

In Figs. 19–28, we present only plots of the final optimized crystal structures and the corresponding band structures for the 6th through 10th optimized bandgaps for TE and TM polarizations. We see that the optimized TM band gaps are exhib-

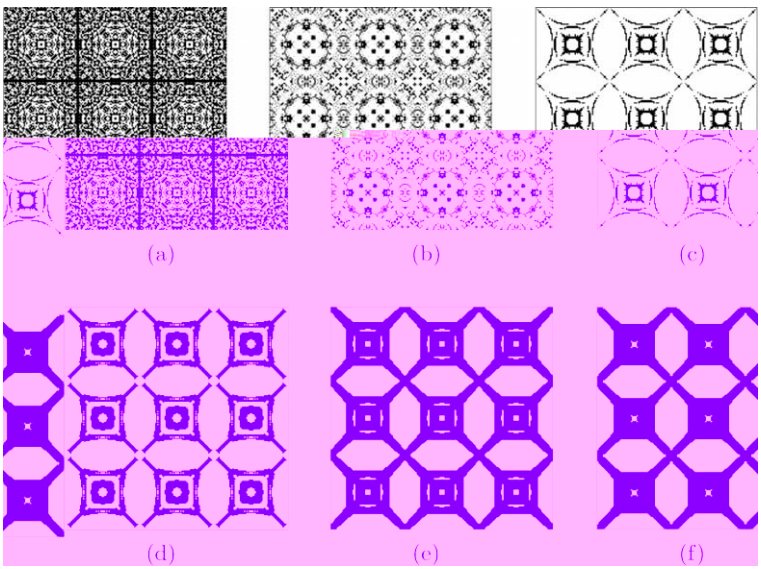

Fig. 17. The evolution of the square lattice crystal structure for optimizing the gap–midgap ratio between $\lambda^{3}_{\mathrm{TE}}$ and $\lambda^{4}_{\mathrm{TE}}$.

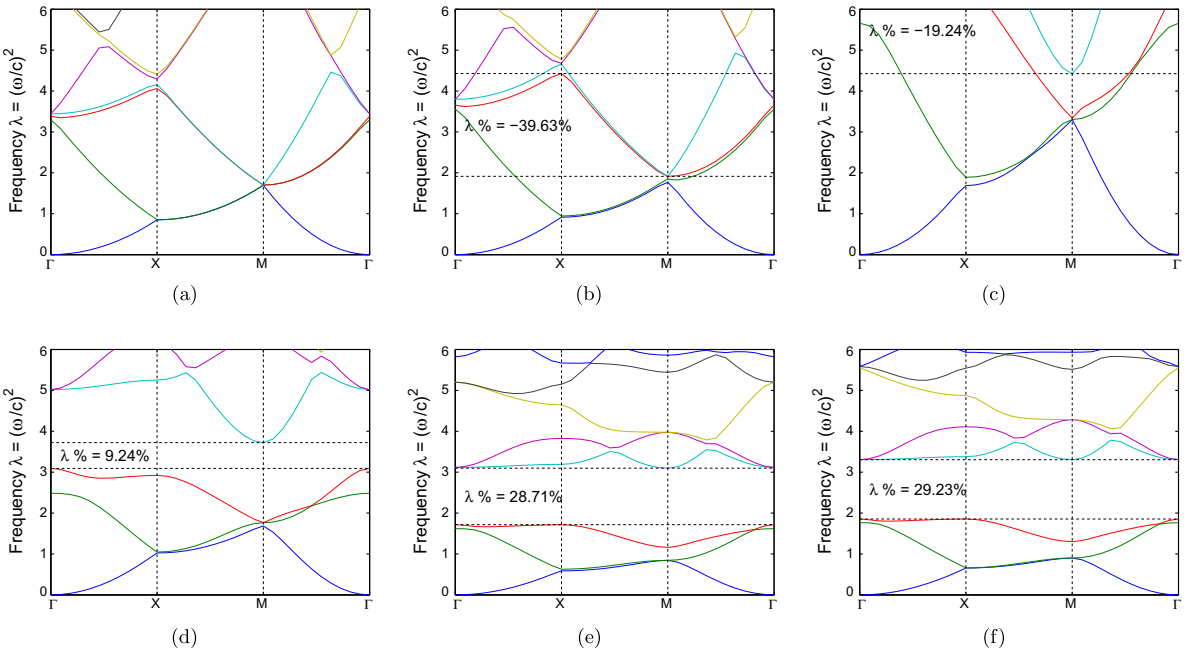

Fig. 18. The corresponding band structure (of Fig. 17) and the gap–midgap ratio between λ^3_{TE} and λ^4_{TE} in the square lattice.

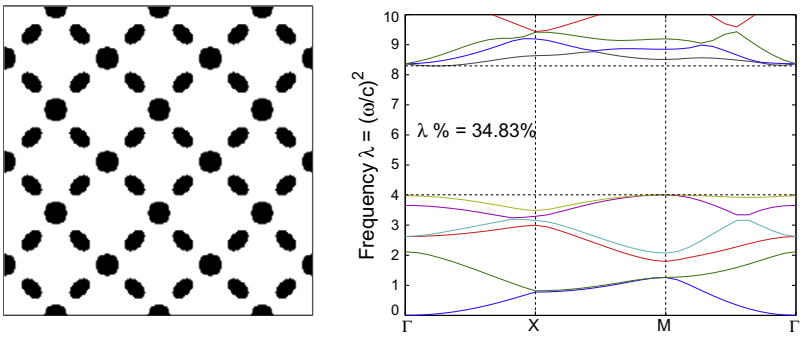

(a) Optimal crystal structure (b) Optimal band structure

Fig. 19. Optimization of bandgap between λ^6_{TM} and λ^7_{TM} in the square lattice.

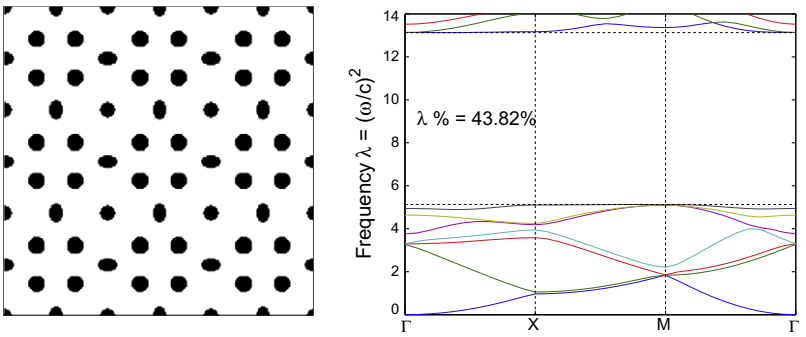

(a) Optimal crystal structure (b) Optimal band structure

Fig. 20. Optimization of bandgap between λ^7_{TM} and λ^8_{TM} in the square lattice.

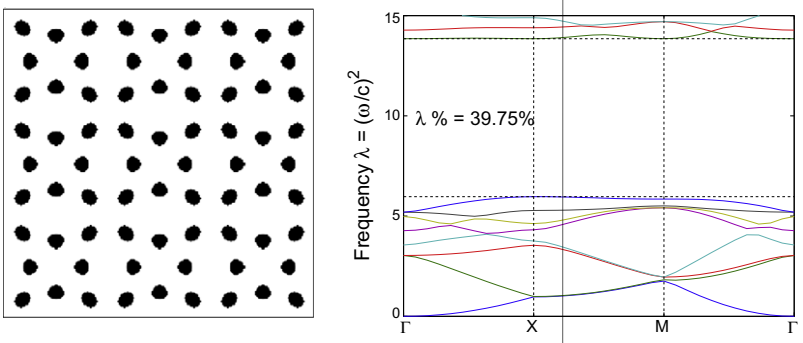

(a) Optimal crystal structure (b) Optimal band structure

Fig. 21. Optimization of bandgap between λ^8_{TM} and λ^9_{TM} in the square lattice.

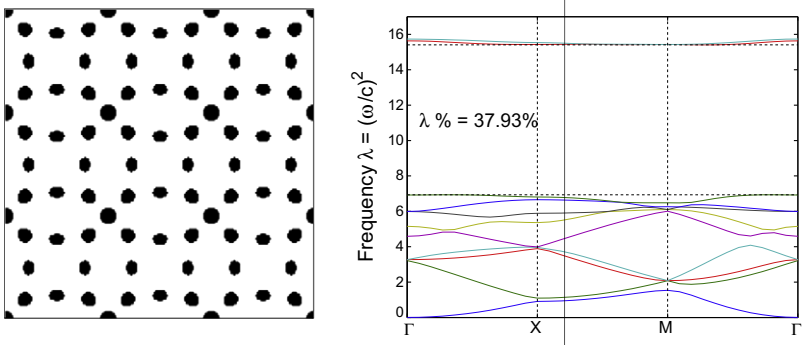

(a) Optimal crystal structure (b) Optimal band structure

Fig. 22. Optimization of bandgap between λ^9_{TM} and λ^{10}_{TM} in the square lattice.

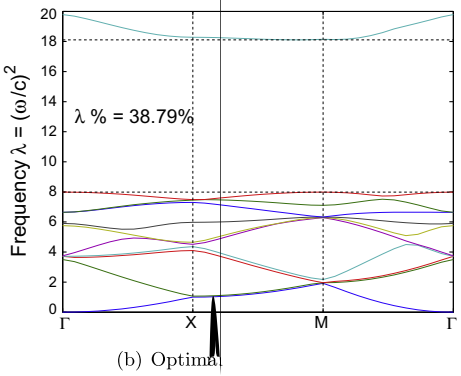

(a) Optimal crystal structure (b) Optima

ited in isolated high-ε structures, while the optimized TE bandgaps appear in connected high-ε structures. This observation has also been pointed out in [13] (p75) "*the TM bandgaps are favored in a lattice of isolated high-$\boldsymbol{\varepsilon}$ regions, and TE bandgaps are favored in a connected lattice*", and observed in [15] previously. For both TE and TM polarizations, the crystal structures become more and more complicated as we progress to higher bands. It would be very difficult to create such structures using physical intuition alone. The largest gap–midgap ratio for the TM case is 43.82% between the seventh and eighth

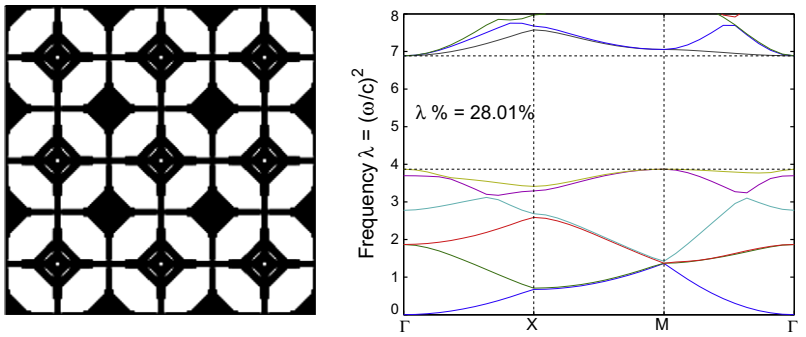

(a) Optimal crystal structure (b) Optimal band structure

Fig. 24. Optimization of bandgap between λ_{TE}^{6} and λ_{TE}^{7} in the square lattice.

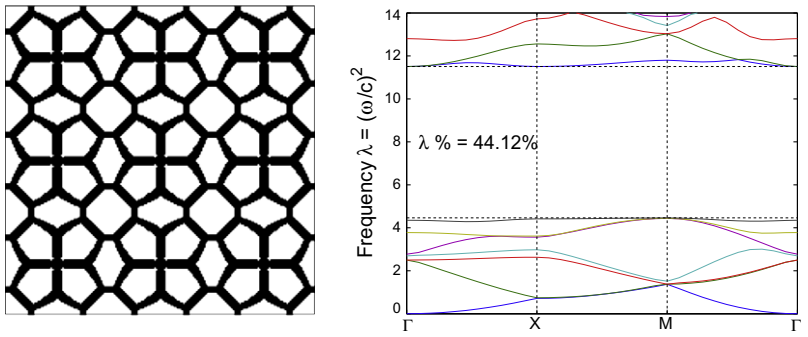

(a) Optimal crystal structure (b) Optimal band structure

Fig. 25. Optimization of bandgap between λ_{TE}^{7} and λ_{TE}^{8} in the square lattice.

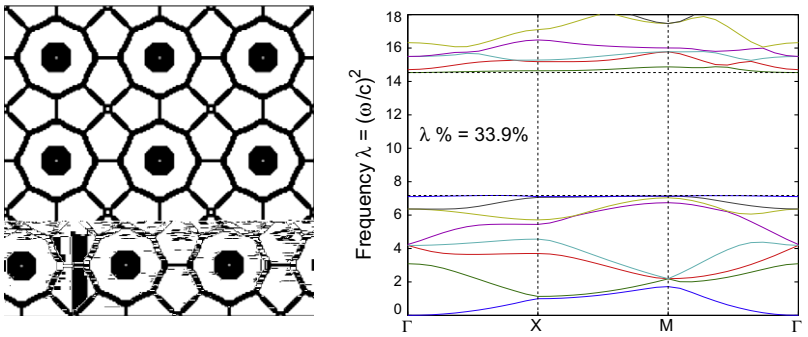

(a) Optimal crystal structure (b) Optimal band structure

Fig. 26. Optimization of bandgap between λ_{TE}^{8} and λ_{TE}^{9} in the square lattice.

frequency bands, while the largest ratio for the TE case is 44.12%, also between the seventh and eighth bands. The results presented here are not guaranteed to be globally optimal, as pointed out in Section 4.2.1. While most crystal structures in the TM cases appear similar to those presented in [15], we have shown quite different TE structures. A qualitative comparison between the two results in the background indicates larger bandgaps (both in absolute value and in the gap–midgap ratio) in our results.

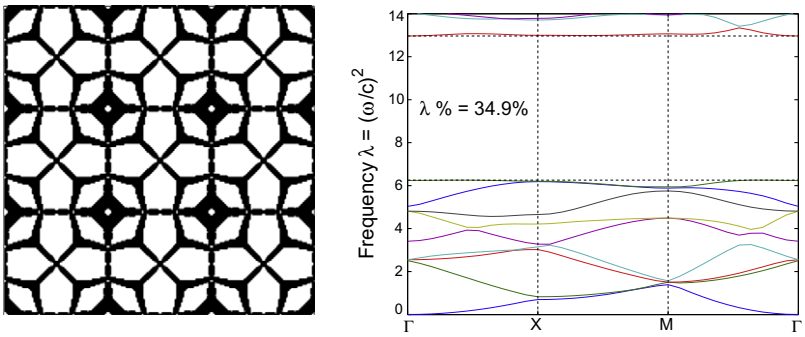

(a) Optimal crystal structure (b) Optimal band structure

Fig. 27. Optimization of bandgap between λ_{TE}^{9} and λ_{TE}^{10} in the square lattice.

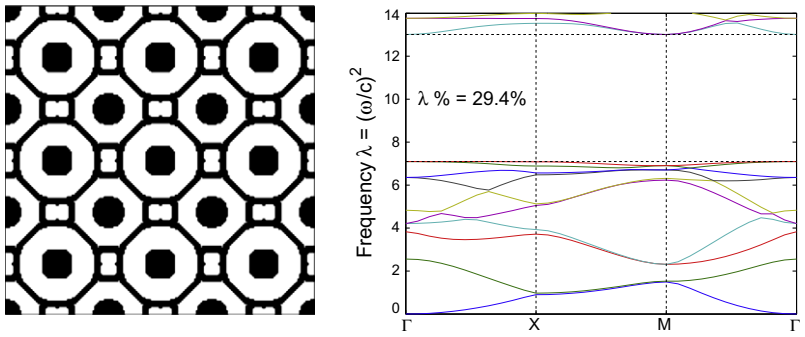

(a) Optimal crystal structure (b) Optimal band structure

Fig. 28. Optimization of bandgap between λ_{TE}^{10} and λ_{TE}^{11} in the square lattice.

5. Conclusions and future work

We have introduced a novel approach, based on reduced eigenspaces and semidefinite programming, for the optimization of bandgaps of two-dimensional photonic crystals on square lattices. Our numerical results convincingly show that the proposed method is very effective in producing a variety of structures with large bandgaps at various frequency levels in the spectrum.

Since our computational techniques make essential use of the finite element method, we anticipate that notions of mesh adaptivity can be easily incorporated into our approach, and thus its computational efficiency will be improved even further. For example, one can start with a relatively coarse mesh and converge to a near-optimal solution, and then judiciously refine the finite element mesh (e.g., refining elements at the interface of dielectric materials) using the current optimal solution at the coarser mesh as the new initial configuration. We intend to explore this approach and report the details and results in a forthcoming paper.

The main strengths of our proposed approach to solve eigenvalue gap optimization problem is the fact that SDP-based methods do not require explicit computation of (sub-)gradients of the objective function (which are ill-defined in the case of eigenvalue multiplicities), hence maintaining the regularity of the formulation. The approach proposed in this paper can also be readily extended to deal with more general problems, such as the optimization of photonic crystals in combined TE and TM fields, optimizing multiple bandgaps, dealing with other types of lattices (e.g. triangular), as well as modeling and optimizing the design of three-dimensional photonic crystals.

Acknowledgments

We are grateful to Professor Steven Johnson of the Mathematics Department of MIT for numerous discussions on this research. We thank Professor Lim Kian Meng of National University of Singapore for advising and supporting of H. Men. We are grateful to the anonymous reviewers of this paper for their suggestions on improving the paper.

References

[1] F. Alizadeh, Interior point methods in semidefinite programming with applications to combinatorial optimization, SIAM Journal on Optimization 5 (1) (1995) 13–51.

[2] F. Alizadeh, J.P.A. Haeberly, M.L. Overton, Primal–dual interior-point methods for semidefinite programming: convergence rates, stability and numerical results, SIAM Journal on Optimization 8 (3) (1998) 746–768.
[3] F. Bloch, Über die quantenmechanik der elektronen in kristallgittern, Zeitschrift für Physik A Hadrons and Nuclei 52 (7) (1929) 555–600.
[4] M. Burger, S.J. Osher, E. Yablonovitch, Inverse problem techniques for the design of photonic crystals, IEICE Transactions on Electronics E Series C 87, 258–265.
[5] E. Cances, C. LeBris, N.C. Nguyen, Y. Maday, A.T. Patera, G.S.H. Pau, Feasibility and competitiveness of a reduced basis approach for rapid electronic structure calculations in quantum chemistry, in: Proceedings of the Workshop for High-dimensional Partial Differential Equations in Science and Engineering (Montreal), vol. 41, 2007, pp. 15–57.
[6] A. Charnes, W.W. Cooper, Programming with linear functionals, Naval Research Logistics Quarterly 9 (1962).
[7] S.J. Cox, D.C. Dobson, Band structure optimization of two-dimensional photonic crystals in H-polarization, Journal of Computational Physics 158 (2) (2000) 214–224.
[8] B.D. Craven, B. Mond, The dual of a fractional linear program, Journal of Mathematical Analysis and Applications 42 (3) (1973) 507–512.
[9] M. Doosje, B.J. Hoenders, J. Knoester, Photonic bandgap optimization in inverted fcc photonic crystals, Journal of the Optical Society of America B 17 (4) (2000) 600–606.
[10] S. Fan, J.D. Joannopoulos, J.N. Winn, A. Devenyi, J.C. Chen, R.D. Meade, Guided and defect modes in periodic dielectric waveguides, Journal of the Optical Society of America B 12 (7) (1995) 1267–1272.
[11] S. Fan, P. Villeneuve, J. Joannopoulos, H. Haus, Channel drop filters in photonic crystals, Optics Express 3 (1) (1998) 4–11.
[12] G. Floquet, Sur les equations differentielles lineaires a coefficients periodiques, Ann De L'ecole Normale Superieure 2 (12) (1883) 47–88.
[13] J.D. Joannopoulos, S.G. Johnson, J.N. Winn, R.D. Meade, Photonic Crystals: Molding the Flow of Light, Princeton University Press, 2008.
[14] S. John, Strong localization of photons in certain disordered dielectric superlattices, Physical Review Letters 58 (23) (1987) 2486–2489.
[15] C.Y. Kao, S. Osher, E. Yablonovitch, Maximizing band gaps in two-dimensional photonic crystals by using level set methods, Applied Physics B: Lasers and Optics 81 (2) (2005) 235–244.
[16] Y. Nesterov, A. Nemirovskii, Interior-point polynomial algorithms in convex programming, SIAM Studies in Applied Mathematics 13 (1994).
[17] G.S.H. Pau, Reduced-basis method for band structure calculations, Physical Review E (Statistical, Nonlinear, and Soft Matter Physics) 76 (4) (2007) 046704.
[18] L. Rayleigh, On the maintenance of vibrations by forces of double frequency, and on the propagation of waves through a medium endowed with a periodic structure, Philosophical Magazine 24 (147) (1887) 145–159.
[19] O. Sigmund, K. Hougaard, Geometric properties of optimal photonic crystals, Physical Review Letters 100 (15) (2008) 153904.
[20] O. Sigmund, J.S. Jensen, Systematic design of phononic band-gap materials and structures by topology optimization, Philosophical Transactions: Mathematical, Physical and Engineering Sciences (2003) 1001–1019.
[21] M. Soljacic, S.G. Johnson, M. Ibanescu, Y. Fink, J.D. Joannopoulos, Optimal bistable switching in nonlinear photonic crystals, Physical Review E 66 (2002) 055601.
[22] R.H. Tütüncü, K.C. Toh, M.J. Todd, Solving semidefinite-quadratic-linear programs using SDPT3, Mathematical Programming 95 (2) (2003) 189–217.
[23] L. Vandenberghe, S. Boyd, Semidefinite programming, SIAM Review 38 (1) (1996) 49–95.
[24] H. Weyl, Symmetry, Princeton University Press, 1952.
[25] H. Wolkowicz, R. Saigal, L. Vandenberghe, Handbook of Semidefinite Programming: Theory, Algorithms, and Applications, Kluwer Academic Publishers, 2000.
[26] E. Yablonovitch, Inhibited spontaneous emission in solid-state physics and electronics, Physical Review Letters 58 (20) (1987) 2059–2062.
[27] X.L. Yang, L.Z. Cai, Y.R. Wang, C.S. Feng, G.Y. Dong, X.X. Shen, X.F. Meng, Y. Hu, Optimization of band gap of photonic crystals fabricated by holographic lithography, EPL-Europhysics Letters 81 (1) (2008) 14001.
[28] M.F. Yanik, S. Fan, Stopping and storing light coherently, Physical Review A 71 (1) (2005) 013803. Jan.